**An-Najah National University**
**Faculty of Graduate Studies**

# CHARACTERIZATION OF DAMAGE IN ALUMINUM NITRIDE SINGLE CRYSTALS BY RBS-C, AN ION BEAM ANALYSIS TECHNIQUE

**By**
**Sarab Awwad Hussein**

**Supervisors**
**Prof. Ismail Warad**
**Dr. Ahmed Bassalat**

**This Thesis is Submitted in Partial Fulfillment of the Requirements for the Degree of Master of Chemistry, Faculty of Graduate Studies, An-Najah National University, Nablus – Palestine.**

**2024**

# CHARACTERIZATION OF DAMAGE IN ALUMINUM NITRIDE SINGLE CRYSTALS BY RBS-C, AN ION BEAM ANALYSIS TECHNIQUE

**By**
**Sarab Awwad Hussein**

This Thesis was defended successfully on 20/10/2024 and approved by:

| | |
|---|---|
| Prof. Ismail Warad | |
| Supervisor | Signature |
| Dr. Ahmed Bassalat | |
| Co-Supervisor | Signature |
| Prof. Atef Qasrawi | |
| External Examiner | Signature |
| Dr. Ismail Badran | |
| Internal Examiner | Signature |

# Dedication

Praise be to God Almighty, Lord of the worlds before and after, I dedicate this thesis to my beloved parents, my siblings, especially my brother Mohammed, and to the memory of my sister Hanan. I also dedicate this work to my wonderful husband Omar.

Especially dedicated to my amazing supervisor Aurélie, and to all the professors and doctors who taught me; to everyone who provided opportunities and believed in me; to my friends and everyone who left a mark on my educational journey.

# Acknowledgments

First, I praise and thank Allah for guiding me on the right path.

I am grateful to An-Najah National University for the opportunity to participate in the Erasmus+ program, allowing me to conduct my thesis research at Paris-Saclay University. Special thanks to IJCLab for welcoming me into their team.

I deeply appreciate my supervisor, Dr. Aurélie Gentils, Scientific Leader of the JANNuS-SCALP facility, and my co-supervisor, Prof. Frédéric Garrido from Université Paris-Saclay, for their exceptional guidance and support. Their mentorship has been crucial to my research's direction and success.

The experimental work for this research took place at IJCLab from May 9 to July 29, 2023. Dr. Gentils and Prof. Garrido's mentorship, insightful feedback, and support were vital to my work during this time. I am also grateful to my supervisor, Prof. Ismail Warad, and to Dr. Ahmed Bassalat and Dr. Hadil Abualrob for offering me the chance to be part of their team in France.

I would like to thank my group at IJCLab, especially Gabriel and Mohammed, for their help and encouragement, and Florian Pallier and the technical staff at the SCALP facility.

I am profoundly grateful to my family, especially my parents, brother Mohammed, and sister Dr. Shaima, for their constant love and support. Special thanks to my friends Shaima and Attaa for their encouragement.

Finally, my deepest gratitude goes to my husband, Omar, for his unwavering love and support throughout this journey.

Sarab A. Hussein

## Declaration

I, the undersigned, declare that I submitted the thesis entitled:

# CHARACTERIZATION OF DAMAGE IN ALUMINUM NITRIDE SINGLE CRYSTALS BY RBS-C, AN ION BEAM ANALYSIS TECHNIQUE

I declare that the work provided in this thesis, unless otherwise referenced, is the researcher's own work, and has not been submitted elsewhere for any other degree or qualification.

Student's Name Sarab Awwad Hussein

Signature: 

Date: 20/10/2024

# List of Contents

# List of Tables

# List of Figures

## List of Schemes

# CHARACTERIZATION OF DAMAGE IN ALUMINUM NITRIDE SINGLE CRYSTALS BY RBS-C, AN ION BEAM ANALYSIS TECHNIQUE

**By**
**Sarab Awwad Hussein**
**Supervisors**
**Prof. Prof. Ismail Warad**
**Dr. Ahmed Bassalat**

## Abstract

Insulating optical materials such as aluminum nitride (AlN) will play a crucial role in future fusion reactors, particularly in diagnostic systems. AlN is being considered as an insulating coating in some reactor designs due to it is high resistance to chemical corrosion and also exhibits a high thermal conductivity up to 321 W/(m·K). Understanding the degradation mechanisms of AlN under implantation and irradiation is of utmost importance.

This study investigated the effect of helium ions on the structure of aluminum nitride (AlN) single crystals using 6 MeV $Au^+$ ions. The crystals were implanted with $Au^+$ ions and analyzed using the Rutherford Backscattering in Channeling (RBS/C) technique across various ion fluences to mimic damage from heavy recoil nuclei. Results showed a gradual increase in damage, measured as a percentage of defects, with increasing ion fluences, reaching saturation at a depth of around 1.3 μm. Monte Carlo McChasy simulations validated the experimental Rutherford Backscattering in Channeling RBS/C data, demonstrating excellent agreement.

Transmission electron microscopy (TEM) observations of AlN samples pre-implanted with 6 MeV $Au^+$ ions at room temperature revealed a gradient of defect concentration, with higher densities at the rear of the damaged layer and notably high defect density at the surface. Discrepancies between observed defect sizes and the Stopping and Range of Ions in Matter (SRIM) predictions highlighted SRIM's limitations for high-energy, high-mass projectiles on light targets. X-ray diffraction (XRD) analysis provided insights into strain values influenced by implantation fluence and flux. Despite a slight temperature increase in the highest fluence sample, strain values remained consistent with lower fluences, indicating robust behavior. Elastic strains increased with fluence, reaching saturation at approximately 1.7% and 2.5% for near-surface and peak damage regions,

respectively. Challenges in determining near-surface strain due to complex XRD curve shapes were noted, but an overall trend was observed

This study offers valuable insights into the structural changes induced by helium in AlN crystals, enhancing our understanding of material responses to irradiation and aiding in the development of predictive models for radiation-induced damage in materials.

**Keywords:** aluminum nitride crystals; Ion implantation; Rutherford backscattering spectroscopy-channeling (RBS/C), Monte Carlo simulation McChasy code; Defects; Strain; $He^{+}$; $Au^{+}$ ions.

# Chapter One
# Introduction

## 1.1 Nuclear Reactors for Electricity Production

For decades modern societies have been developing and searching for various technologies to cover energy demands, and among those, is one of the most important technologies is nuclear reactors. Nuclear reactor technology, which started for research applications in the 1940s, and electricity was generated for the first time from nuclear energy in 1951, stands out as an exceptional source of power. These complicated systems operate through controlled nuclear reactions, primarily involving fusion and fission processes; nuclear reactions are initiated, managed, and directed to take advantage of the enormous energy stored within the atomic nuclei [1].

The nuclear reactor produces and controls the release of energy from splitting atoms of certain elements. The core of a nuclear reactor consists of fuel rods, each containing fissile material mostly uranium-235 or plutonium-239. The reactor operates on the principles of chain reactions [1][2]. In nuclear fission, the nucleus of a heavy atom is bombarded with a neutron, and the nucleus splits into smaller fragments, releasing large amounts of energy, for example, the approximate energy released from the uranium-235 fission reaction is 200 MeV in terms of kinetic energy (heat). The released energy is computed by Einstein's equation.

$$E = mc^2 \qquad (1)$$

Where E, m, and c represent the total energy of a nucleus, its mass, and the speed of light, respectively. This process also releases additional neutrons, these released neutrons in another step collide with other fissile nuclei, perpetuating the chain reaction [3].

Fission is the process behind the operation of the existing nuclear power plants, where controlled chain reactions occur in the reactor core, generating heat that is used to produce steam which drives turbines to generate electricity for various applications [2].

In contrast to fission reaction, nuclear fusion reaction involves combining light atomic nuclei, mostly isotopes of hydrogen, to form a heavier nucleus, for example, the reaction

between deuterium ($^{2}H$) and tritium ($^{3}H$) that yields helium ($^{4}He$) and a neutron ($^{1}n$), this process releases an enormous amount of energy.

The fusion reaction is the process that powers the sun and other stars [2]. On Earth, achieving controlled fusion has proven to be challenging due to the extreme conditions required, such as high temperatures and pressures. Successful fusion could offer a nearly limitless and clean source of energy due to its lack of greenhouse gas emissions, minimal long-lived radioactive waste, it produces no air pollution, has a high energy yield, and poses no meltdown risks, as reactions stop automatically if containment fails, but as of now, sustained and controlled fusion reactions are still being researched and developed [4].

Although fusion's challenges are enormous, including achieving and maintaining the extreme conditions required for fusion reactions, many projects are investing in this field. The International Thermonuclear Experimental Reactor (ITER) project is an international scientific project funded and operated by seven member parties. These members are China, the European Union, India, Japan, Russia, South Korea, and the United States. The project is based in France and aims to demonstrate the feasibility of controlled fusion on a global scale [5].

As a comparison between nuclear fission and fusion, fission is one of the most important technologies for power generation. It offers practical applications, but it generates long-lived radioactive waste and increases the risk of nuclear waste increase. On the other hand, fusion promises a nearly boundless and clean energy source, generating less radioactive waste than fission. However, achieving fusion reactions remains an ongoing scientific and engineering challenge [4][6].

The usage of nuclear fission to generate energy is very common in many countries, for instance, the United States of America has 92 commercial reactors that produce a substantial portion of its electricity from nuclear sources, contributing to its energy security and low-carbon energy. France stands out as a pioneer in nuclear energy, with 70% of its electricity generated by nuclear fission energy, emphasizing its commitment to clean energy. Russia too is a major player in nuclear power generation [7].

Nuclear reactions including fission and fusion, release various types of ionizing radiation including alpha particles (α), beta particles (β), and gamma rays (γ).

Alpha particles consist of two protons and two neutrons and when they're produced it's called alpha decay. Due to their relatively large mass, they have limited penetration capability, these particles can be stopped by a sheet of paper or even human skin. However, particles could carry high kinetic energy, upon colliding with a material, which can disrupt atomic bonds and create defects in the material's structure. Yet, the limited range of alpha particles typically borders their damage to the surface layer of the material. Furthermore, it is also the most ionizing form of radiation compared to others [8].

Beta radiation consists of high-energy electrons or positrons (the antiparticle of an electron), and it has a greater penetration capacity compared to alpha particles. The damage they cause is similar to that of alpha but on a broader scale, as beta particles break through further, they interact with more atoms, leading to a wider range of atomic displacements and defects. Beta particles can cause ionization in both living tissues and materials. Although beta radiation can be blocked by materials like clothing or plastic, it still can break through the skin, potentially causing burns or cellular damage [8].

Gamma Rays are photons with no mass and no charge that carries electromagnetic energy propagating with a velocity equal to the speed of light. Since gamma rays are a form of electromagnetic waves, it is capable of substantial breakthroughs through most materials, including human tissue. As gamma rays pass through, they ionize atoms and molecules along their path, creating cascades of secondary radiation, this secondary radiation can cause widespread damage within the material, leading to the creation of defects, changes in a crystalline structure, and overall degradation of mechanical properties. They can also cause ionization and cellular damage, posing significant health risks, especially for long exposure duration [8].

These reactions emit various types of ionizing radiation, each possessing unique breakthrough capabilities and biological effects, the impact of radiation on nuclear materials depends on the type of radiation and nuclear material. Types of radiation with different penetration levels shown in Figure 1.1.

**Figure 1.1**

*Different penetration levels for different types of radiation, with alpha showing the lowest penetrating level and gamma being one of the most highly penetrating*

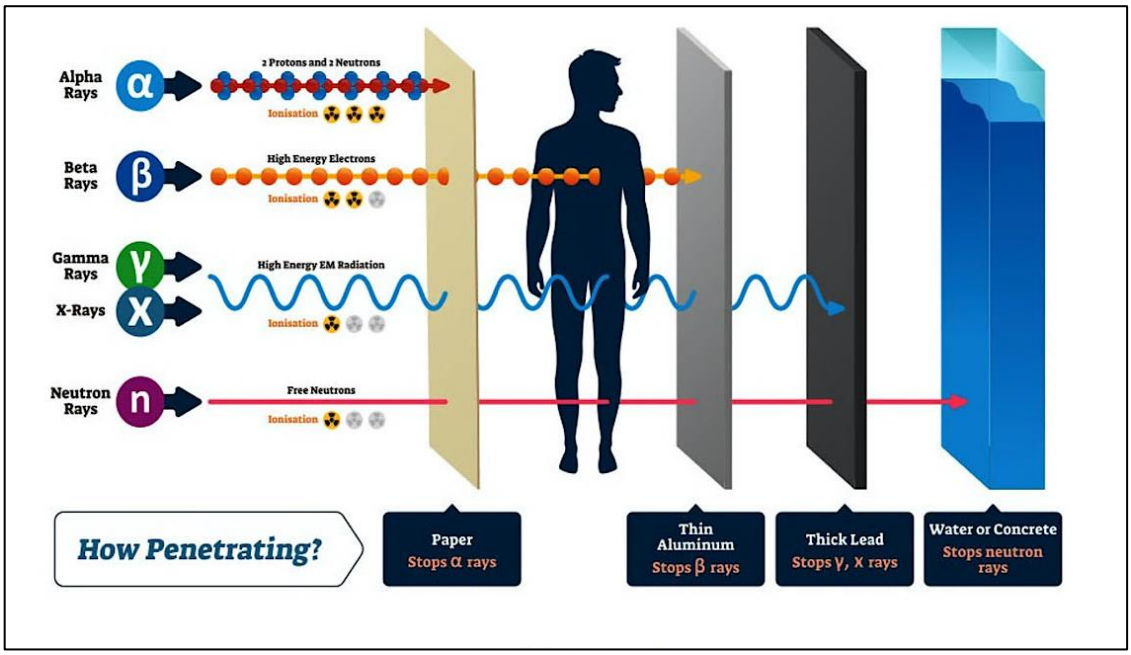


Note: Energy Education. (2022).

Due to the high penetration capability of these radiations within materials and their potential to induce significant structural damage in materials used in reactors, including atoms being displaced from their regular positions, leading to the formation of vacancies in the material's structure, these defects can change the mechanical, and the thermal properties of the materials, potentially making it more brittle, less flexible, and less thermally conductive [10].

This research project will concentrate on the materials used in fusion reactors, with a particular emphasis on exploring the impacts caused by neutrons and the buildup of gasses, like helium and hydrogen. These factors can have significant consequences on the properties and structural soundness of materials in the demanding environment of fusion reactors. The study will explore the intricate relationship between gas accumulation and irradiation damage to enhance the durability and efficiency of these materials.

## 1.2 Nuclear materials

The development of high-performance materials for energy generation, containment, and storage has become a key factor for more sustainable management of the ever-growing demand for electrical power. Depending on the applicability, certain material's physical

properties will have to be analyzed and enhanced to boost safety, long-term use, or energy conversion efficiency on specific applications. In nuclear technology, other materials are needed to moderate the reaction and prevent radiation leakage besides fissile materials like uranium and plutonium pellets that sustain chain reactions that generate energy. These latter materials need to be radiation tolerant while maintaining good mechanical and corrosion resistance [11].

In the case of thermoelectric technology, the materials that will be used to convert heat into electricity need to have good electric transport properties and poor thermal conductivity. In the case of combined nuclear-thermopower applications, they also maintain their integrity in a harsh radiation environment. Nuclear materials are a characteristic class of solid substances that steadily face an extremely hard environment of radiation sources and potential additional thermodynamic conditions, including temperature, pressure, and chemical agents. The complex interaction of these factors creates a challenge in understanding and estimating material behavior under radiation [9]. Examples of nuclear materials: the nuclear fuel (uranium dioxide in fission PWR), structural materials (often steels, zirconium-based alloys, tungsten in fusion), ceramics and glasses for nuclear waste management, and polymers.

Nuclear materials have a wide range of applications. They are used in medical treatments and imaging to monitor and treat metabolic processes or tissues in humans. Similarly, they are also used in veterinary treatments to cure animals. In industries, nuclear materials are used in different devices such as irradiators, gauging devices, well-logging devices, and industrial radiography systems. Additionally, academic institutions such as universities and colleges use nuclear materials for coursework, laboratory demonstrations, and research purposes [12].

Silicon (Si) and Gallium (Ga) elements both hold significance in this field due to their unique properties and high-potential applications. Indeed, the importance of silicon as a semiconductor in nuclear technology cannot be overstated, as it plays a critical role in detecting and responding to ionizing radiation, making it an essential component of radiation detection equipment, and in nuclear environments, accurate monitoring, and evaluation of radiation levels hinge on the reliable performance of this indispensable material. Additionally, silicon's stability at elevated temperatures and corrosion resistance

makes it suitable for use in cladding materials for nuclear fuel rods, contributing to the structural integrity of reactor systems [13].

Gallium, on the other hand, with its unique characteristics makes (Ga) a good material for use in the nuclear industry, with its low melting point and liquid-state properties, gallium is ideal for applications involving liquid metal coolants in advanced reactor designs [11].

Also, Aluminum Nitride ($Al \equiv N$) is one of the most promising materials in nuclear applications, especially for fusion applications due to its excellent mechanical properties, chemical inertness, and high melting point. The AlN is suitable to operate in high temperatures and harsh environmental conditions and therefore is very promising to be employed in industrial applications [14].

### 1.2.1 Damages (defects) in nuclear materials produced by ion irradiation and implantation

Irradiations in reactors induce damage to materials. At the nanoscale, a crystallographic defect refers to the disruption of the typical arrangement of atoms or molecules in crystalline solids. The interaction of accelerated particles with the target's atoms leads to the target's microstructure modification, and thus to a modification of their physical and chemical properties. In nuclear materials, for example, exposure to energetic particles can cause nuclear materials to weaken, leading to a decrease in their lifespan. Similarly, when semiconductor materials undergo ion implantation or irradiation, The defects that form can significantly alter the material's electrical and thermal properties [15].

The interactions of energetic particles with a target generate collision cascades that will give rise to atomic displacements and defects. Heavier particles, such as neutrons and heavy ions produce denser collision cascades when compared to particles and/or light ions, facilitating the accumulation of point defects. Moreover, the material will have temperature effects depending on the cascade density.

Ion implantation can produce defects such as dislocation loops, precipitates, atomic clusters, and Frenkel pairs. This defect forms when an atom or smaller ion (usually a cation) leaves its place in the lattice, creating a vacancy (an empty lattice site ), and becomes an interstitial by lodging in a nearby location, which interstitial is atoms were

knocked out of their original site, and come to stop in the solid. In some special cases, the vacancy may be re-occupied with new atoms identical to their original atom and this is called Replacement Collision. Although this may sound complicated, this mechanism may reduce the total vacancies by up to 30%. [16].

However, the damage and transformation of a material's structure can lead to various changes in its properties, such as swelling, local amorphization, and modification of chemical, electronic, thermal, and mechanical characteristics. Some examples of implantation-induced defects are presented in Figure 1.2.

**Figure 1.2**

*Types of implantation-induced defects inside a crystal, including Frenkel pairs (vacancy, interstitial), dislocation loops, precipitates, and atomic clusters*

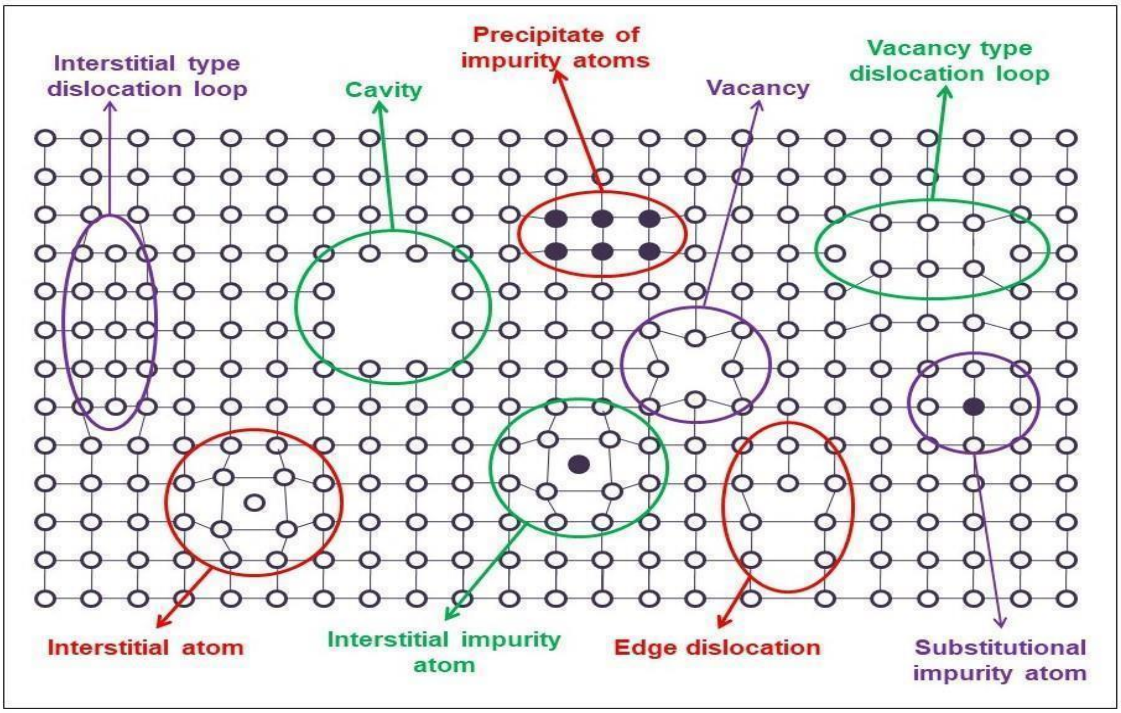


Note: *Each circle is an atom.* Meissner, & Medjdoub, (2024).

### 1.2.2 Ceramics

Ceramics have gained significant attention in the realm of nuclear materials due to their exceptional combination of properties that make them well-suited for challenging nuclear environments. These inorganic, non-metallic materials exhibit excellent thermal stability, corrosion resistance, and remarkable radiation tolerance, making them ideal candidates for various nuclear applications [18].

In nuclear reactors, ceramics are essential structural materials that can withstand high temperatures and harsh radiation conditions while retaining their mechanical integrity.

Zirconium dioxide (  ), and silicon carbide ( 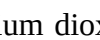 ) are exceptional examples of ceramics used in nuclear reactor components. Their unique ability to endure extreme conditions, coupled with their low neutron absorption characteristics, significantly enhances the safety and longevity of nuclear reactors.

Furthermore, ceramics play a crucial role in the production and containment of nuclear fuel, contributing significantly to the overall efficiency and reliability of the nuclear energy generation process. Their remarkable versatility and flexibility make them indispensable materials in the field of nuclear science and technology [18].

A promising category of ceramics for use as structural radiation-resistant materials includes nitride ceramics such as AlN, $Si_3N_4$, TiN, and ZrN, with AlN being particularly noteworthy. The interest in these materials arises from their distinctive properties.

### 1.2.2.1 Aluminum nitride (AlN)

In the quest for technological advancements, aluminum nitride (AlN) has become a transformative component with a profound impact across various sectors.

AlN, a covalently-bonded ceramic, is synthesized from the abundant elements aluminum and nitrogen by the carbothermal reduction of aluminum oxide in the presence of gaseous nitrogen or ammonia or by direct nitridation of aluminum. AlN has a hexagonal structure with strong covalent bonding for crystal and lattice systems; the space group symmetry of AlN is P6_3mc and its point group symmetry is $C_{6v}$, with the dimensions: {a = b = 3.13A°, c = 5.02A°}, and angles alpha = 90°, beta = 90°, and gamma = 120° [19]. See figure 1.3.

AlN is an extremely hard ceramic material with a molar mass of 20.495g/mol, and it has high stability in inert atmospheres at temperatures over 2000°C. Aluminum nitride melts at about 2200 °C, and in a vacuum, AlN decomposes at ~1800 °C. [19] [20]

**Figure 1.3**

*Aluminum nitride (AlN)*

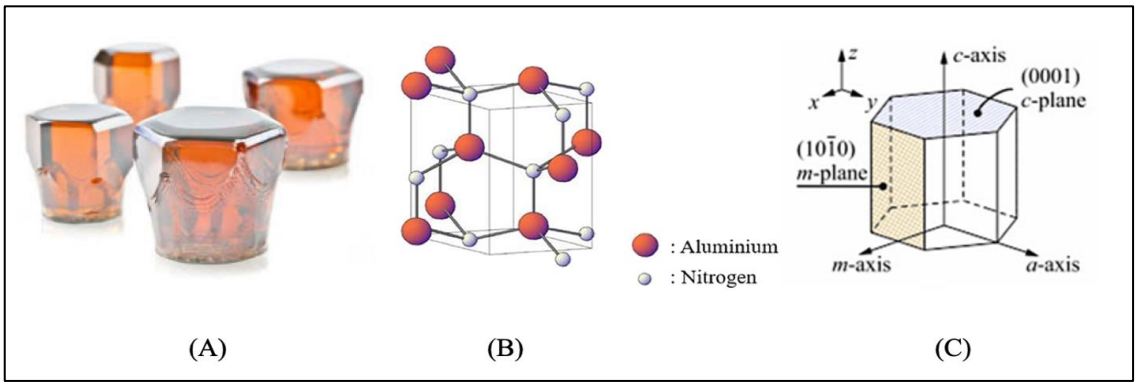


Note: (A) AlN synthesized crystal (B) 3-D AlN crystal construction (C) a typical design of AlN. (Jublot-Leclerc, Bouhali, Pallier, & Declémy, 2021; Hexatech Inc., 2024).

Aluminum nitride (AlN) was chosen as the focus of study over other nitride materials such as $Si_3N_4$, TiN, and BN due to its exceptional tolerance and resistance to radiation damage. Initial experiments demonstrated that AlN could retain its structural integrity under neutron fluence levels as high as $5.8 \times 10^{18}$ n·cm$^{-2}$. Additionally, AlN exhibits remarkable resistance to chemical corrosion and boasts a high thermal conductivity of up to 321 W/(m·K), surpassing that of GaN. Despite these advantages, AlN is recognized as a strong dielectric [21].

The versatility of AlN makes it widely used in various industries. AlN distinguishes itself as a unique material within the semiconductor realm, as it possesses both an exceptionally wide and direct bandgap ($E_{gap}$ = 6.0–6.2 eV), thus its optical absorption/emission in the deep ultraviolet (UV) at ~ 200 nm wavelengths, The bandgap value for SiC and GaN is almost twice that of AlN, while concurrently exhibiting substantial thermal conductivity [23].

AlN serves as a substrate for high-power radio-frequency components and power modules in the electronics industry. Its high thermal conductivity significantly enhances device performance.

AlN is also used in the field of photonics, where it is used in UV light-emitting diodes (LEDs) and photodetectors, leading to advancements in communication and sensing technologies. Furthermore, AlN is a stable in the field of acoustic resonators, sensors, and actuators due to its unique piezoelectric properties. This unusual combination of properties makes AlN a critical advanced material for many future applications in optics,

lighting, electronics, renewable energy, and in the nuclear field as nuclear materials and high-power applications [23].

The present work aims to investigate the influence of helium on the microstructure of aluminum nitride (AlN) single crystals and to test its damage resistance. The effect of helium presence in AlN will be investigated by using helium ion implantation in single crystalline layers of AlN deposited on a substrate. Then it will be characterized by using ion beam analysis techniques to extract the depth distribution of displaced solid atoms as a function of fluence and to monitor possible structural transformations, such as the amorphization of the material at large fluence.

### 1.3 Principles of Microstructure Characterization Techniques

When a material is exposed to irradiation, either internally or through incident particles like ions, electrons, or neutrons, it can undergo various microstructural changes. The accumulation of defects during sustained radiation drives microstructural evolution. These changes can range from simple point defect formation to complex extended defects such as dislocation loops and cavities, and may even result in phase transformations like amorphization in crystalline materials. The choice of techniques to determine the extent of irradiation damage depends on several factors, including the nature and level of the damage, the type of material, and others [24].

There are many techniques used for studying the microstructure of nuclear materials damaged by irradiation that can characterize point defects as vacancies, interstitials, and their associations as Frenkel pairs, but in this study, the focus will be on ion beam analysis techniques, in particular Rutherford Backscattering Spectrometry in the Channelling mode (RBS-C).

#### 1.3.1 Ion Beam Analysis

Ion Beam Analysis (IBA) constitutes a crucial class of modern analytical techniques that employ MeV ion beams for investigating the material composition and acquiring elemental depth profiles within the near-surface layers of solids. All IBA methodologies exhibit remarkable sensitivity, detecting elements down to sub-monolayer levels. Typically, the depth resolution falls within the range of a few nanometers to several tens

of nanometers, with the potential for achieving atomic depth resolution when employing specialized equipment [25].

The analyzed depth spans from a few tens of nanometers to a few tens of micrometers. By using channeling, we can accurately determine the depth profile of damage present in single crystals. Ion beam analysis is based on the principle of bombarding probing ions to a test sample. The interactions between the ions and atoms within the sample lead to the emission of various products. This emission provides valuable data about the quantity, types, distribution, and structural organization of atoms within the sample. To utilize these interactions effectively for determining sample composition, one must carefully select a suitable technique, specify irradiation conditions, and choose an optimal detection system that can isolate the desired radiation while achieving the desired levels of sensitivity and detection limits [26].

#### 1.3.1.1 Rutherford Backscattering Spectrometry in Channeling Geometry (RBS-C)

Rutherford backscattering spectrometry/channeling is a well-established technique based on collisions between atomic nuclei and took its name from Ernest Rutherford's famous explanation of alpha particle scattering from thin gold foil in 1911. This method primarily relies on the measurement of both the quantity and energy of ions that have been backscattered after an elastic collision at a given incident energy and deflection angle with the nuclei located close to the surface of the target material [27].

The energy exhibited by these backscattered ions hinges on several factors:

- Their initial energy upon impact.
- The mass of the target atom they collide with.
- The depth at which this collision interaction occurs.

Backscattering may occur only when the projectile is lighter than the nucleus of an atom. Therefore, RBS experiments are often conducted using helium ions (or protons, deuterons).

In elastic scattering, total kinetic energy is conserved but the projectile loses part of its energy that is given to the target atom. See Figure 1.4.

On the other hand, in an inelastic binary elastic collision, two particles collide and perform a single collision where the projectile transfers energy to the particle. The amount of energy lost depends on the masses of the particles involved [28].

**Figure 1.4**

*The binary collision model describes a collision between a projectile and target atom, resulting in a scattered ion or recoil atom*

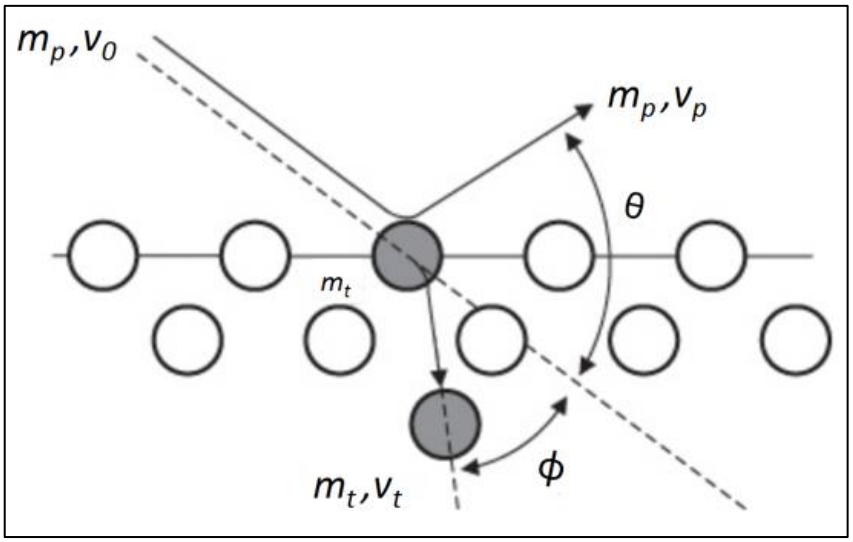


Note: with masses mp and mt, velocities v0, vt, and VP, and angles θ (scattering) and φ (recoil). Salih, (2020).

In the case of a single crystal, the direction of the incident ion beam (helium ion beam) can be chosen to coincide with the direction of the <100> crystal axis. A large number of incident ions then enter the target without encountering any atoms, traveling between the atomic planes, and the elastic backscattering efficiency is therefore very low in this case: this phenomenon is called channeling.

The channeling technique is a valuable tool that utilizes the principles of Rutherford Backscattering (RBS) on a single crystal. Its primary purpose is to investigate crystal damage, defect concentration, and epitaxial crystal alignment. By directing an ion beam along a major crystal axis or plane, the likelihood of ion-atom interaction is significantly reduced. This leads to fewer scattering events and deeper penetration of ions into the crystal. Additionally, the ion flux within the channel undergoes redistribution, which causes a phenomenon referred to as flux-peaking. This results in a higher ion flux at the center of the channel compared to the crystal axis or plane [30]. As a result, when defects are not perfectly located in the crystal lattice, there is a greater chance of backscattering for incoming ions.

The channeling technique is crucial because it enables the observation of well-aligned crystalline lattice site target atoms in the material as rows or planes of periodically repeated atoms between ion channels (see Scheme 1.1). Channeling results in a much lower number of detections of backscattered ions since the majority of ions channel through the crystal with a low probability of being backscattered. This is in contrast to the situation where the ion beam is randomly oriented towards the crystal, where only a small fraction (approximately 1%) of a backscattered event is recorded.

To assess the degree of lattice disorder in a sample, it is possible to record a spectrum with ions channeling the sample and compare the resulting spectrum with that of a crystal exhibiting perfect order or a random spectrum. By doing so, one can obtain a precise measure of the level of disorder present. The RBS/C method is especially valuable for monitoring a sample's depth and degree of lattice disorder [31].

**Scheme 1.1**

*Sketch of the channeling phenomenon*

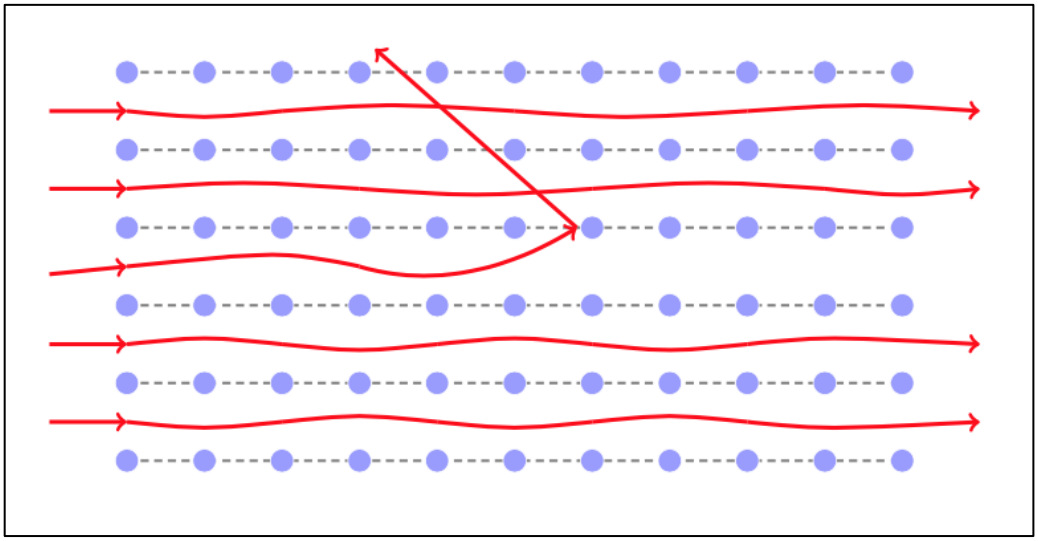

Scheme 1.2 illustrates a typical spectrum obtained by RBS and the channeling technique. The graph shows three different backscattering spectra recorded under distinct conditions. The blue line represents the random spectrum that is obtained when the incident beam is randomly oriented towards the crystal. This configuration yields a relatively high backscattering signal as the probability of the backscattering of incident ions is high. The random spectrum is usually recorded by rotating the crystal around the incident beam at a certain open angle. When an ion beam is directed along the crystallographic orientation

of a flawless crystal (perfect crystal without any defects), the number of backscattering events decreases significantly as most of the ions pass through the crystal without scattering. In this case, only a small fraction of ions may scatter on the lattice atoms, resulting in a low signal in the backscattering spectrum compared to a random spectrum[32].

The green curves in Scheme 1.2 demonstrate this channeling spectrum produced by a non-defective crystal. The ratio of the backscattering yield of the axial channeling spectrum to that of the random spectrum integrated into a specific energy range is called the minimum axial yield ($\chi$min). The theoretical value of $\chi$min for a perfect crystal generally ranges from 1% to 2%, depending on the type of crystal.

If the ion beam is oriented along the crystallographic orientation of a crystal containing defects, the backscattering will be improved as compared to the perfect crystal. As the defects are present in random positions within the crystalline structure, they function as both direct and indirect obstructions to the channeling of the incident beam. The obstruction to the incident ion beam at a given depth from the surface of the crystal is proportional to the local concentration of defect. The crystal-containing defect will result in a higher channeling spectrum compared to the virgin crystal [32].

The red curve in Scheme 1.2 represents the channeling spectrum recorded on a crystal that has defects. The spectrum consists of three main parts: (i) a surface peak caused by ions bouncing back from atoms on the crystal's surface, (ii) a damage peak resulting from ions bouncing back from atoms randomly distributed within the crystal's lattice structure (the level of this peak indicates the concentration of disordered atoms at a specific depth), and (iii) a de-channeling signal due to the small angle.

**Scheme 1.2**

*Typical channeling spectrum of a crystal with defects (red), random spectrum (blue), and channeling spectrum of the perfect crystal (green)*

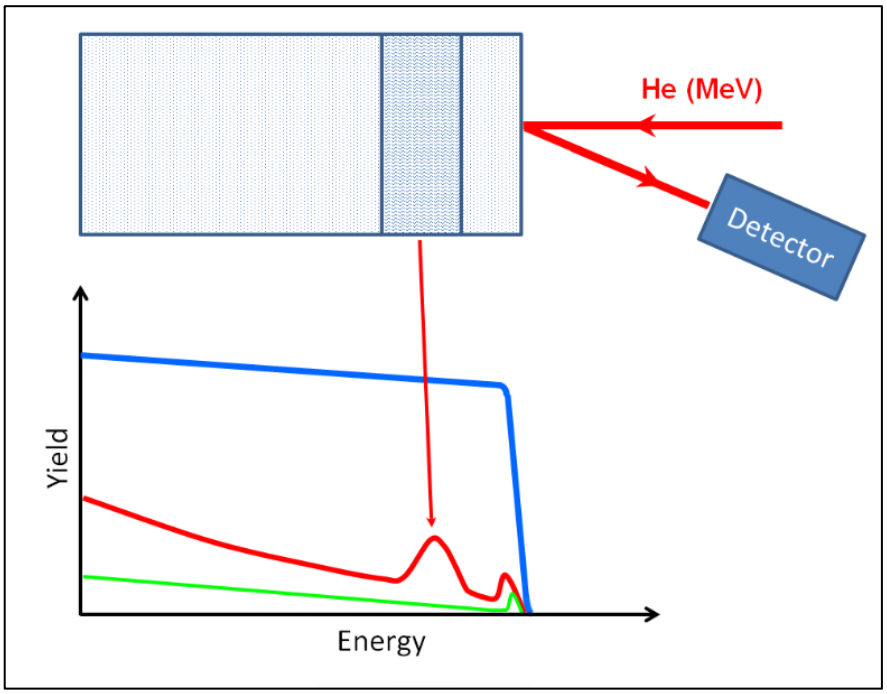


Consequently, the RBS-C technique allows for determining the atomic mass and the concentrations of various elements present in a solid material concerning its depth.

Assuming the conservation of momentum and kinetic energy, the scattered projectile energy, $E_1$ can be expressed as:

$$E_1 = KE_o \tag{2}$$

$$K = \left( \frac{m_1 \cos\theta_1 \pm \sqrt{m_2^{\,2} - m_1^{\,2}(\sin\theta_1)^2}}{m_1 + m_2} \right)^2 \tag{3}$$

Where:

K: the ratio of the projectile energies called the Kinematic factor.

$E_o$: the energy of the incident particle

$m_1$: the mass of the incoming particle

$m_2$: the mass of the target particle

$\theta_1$: the scattering angle in the laboratory, respectively.

For a given $\theta_1$, $m_1$, and $E_o$, the mass of the target atom determines the energy of the backscattered particles. So, in the case of a thin target, the energy spectrum shows several peaks corresponding to the mass of each element that constitutes the target [33].

In addition to the impact of a charged particle on a material, there is also a loss of energy of the projectile ion through electronic excitation when the ion enters and exits the material after backscattering. This additional energy dissipation provides valuable information about the depth at which the collision event takes place. When the backscattering angle is fixed, the analysis of the energies of the ions collected can provide information about the elemental composition of the material and the variations in their concentration beneath the surface [33].

In the energy spectrum, each element is linked to a noticeable peak, whose exact location is determined by the principles of energy and momentum conservation. This is also known as the kinematic factor. Typically, heavier elements are visible at higher energy fronts, while lighter elements are identifiable at lower energy fronts.

RBS/C measurements presented in this experiment were made using helium ions delivered by the ARAMIS accelerator in the JANNuS-Orsay experimental hall of the MOSAIC facility, IJCLab [https://mosaic.ijclab.in2p3.fr]. The characterization beam uses $He^+$ 1.5 MeV as kinetic energy. The He beam was incident along the [0001] direction (c-axis), and the backscattered beam was collected by a detector. RBS/C was conducted at RT.

In addition to the RBS-C technique, there are many characterization techniques as X-ray diffraction (XRD) and transmission electron microscopy (TEM) that are complementary to each other and allow us to better understand the evolution of the microstructure of a material submitted to ion implantation.

#### 1.3.1.2 XRD Technique

X-ray diffraction is an essential technique in the characterization of crystalline materials, providing insight into the lattice parameters and arrangement of individual atoms within a single crystal. It is also useful for analyzing the phase of polycrystalline materials and compounds. Understanding XRD and crystallography enables one to determine the crystal structure and molecular formula of a crystalline compound.

XRD is a valuable non-destructive technique that can work together with other commonly utilized methods such as Rutherford backscattering spectrometry in channeling geometry and transmission electron microscopy to identify and analyze irradiation damage in crystalline samples [34].

XRD operation involves directing an X-ray beam onto the material, resulting in some X-rays interacting with the atoms in the crystal. In various directions, the X-rays will counteract destructively and negate each other. However, in particular directions, the X-rays encourage constructive interference, creating reinforced diffracted X-rays that produce a distinct diffraction pattern. It is these reinforced diffracted X-rays that produce the characteristic X-ray diffraction pattern that is used for crystal structure determination.

While RBS-C provides information on the disorder (fraction of atoms displaced from their site), X-ray diffraction is capable of determining the elastic strains and eventual changes in lattice parameters caused by irradiation-induced defects in single-crystal layers. Point defects, especially interstitial defects, can generate significant elastic strains, thus making the technique highly sensitive to even low levels of damage that may not be detectable by RBS-C or TEM. As a result, X-ray diffraction can detect damage at an earlier stage than other methods [35].

#### 1.3.1.3 TEM Technique

Transmission electron microscopy (TEM) is a popular method for characterizing cavities and extended defects such as dislocations, dislocation loops, and stacking faults. By bypassing an electron beam through the foil of the material of interest, it's possible to obtain local structural and chemical information on a few nanometers or even atomic scale with the latest generation of microscopes. This technique is suitable for characterizing various materials, whether they are metallic or insulating [36].

As an electron beam travels through a sample, it interacts with the material in various ways, such as elastic and inelastic interactions. While some parts of the beam pass through without any deviation, others are deflected by the crystal planes of the material, which is referred to as elastic scattering. Observing the cavities induced by radiation is an essential aspect of characterizing nuclear materials. In TEM, these cavities can be viewed by

defocusing the electron beam. If under-focused, the cavities appear bright with a dark fringe, while if over-focused, they appear dark with a bright fringe [36].

Although transmission electron microscopy (TEM) is a formidable technique, it does have its limitations. Specifically, it can only offer information at a highly localized level. Furthermore, TEM is not proficient in identifying the global disorder. This stands in contrast to the statistical information that can be garnered through methods such as Rutherford backscattering spectroscopy in channeling geometry (RBS-C) or X-ray diffraction (XRD).

### 1.4 Crystallography of AlN

Crystallography is a scientific field that focuses on understanding the arrangement and bonding of atoms in crystalline solids, as well as the geometric structure of crystal lattices.

Crystallography groups are composed of 32 classes of symmetry derived from observations of the external crystal form. From these 32 classes, 230 space groups are distinguishable using x-ray analysis. As mentioned in section 1.2.2.1 AlN has a hexagonal structure with strong covalent bonding for crystal and lattice system; the space group symmetry of AlN is P6_3mc and its point group symmetry is $C_{6v}$, with the dimensions: {a = b = 3.13A°, c = 5.02A°}, and angles (alpha = beta = 90°, and gamma = 120°).

Materials scientists use crystallography to analyze and characterize different materials. In single crystals, the arrangement of atoms is often visible to the naked eye because the natural shapes of crystals reflect the atomic structure. Additionally, physical properties can be influenced by defects in the crystal structure, making it important to understand crystal structures and their defects to know the properties of a material [37].

Crystallography helps predict the crystal's behavior under different conditions, enabling us to explain experimental results accurately. This information is vital for understanding crystal stability, chemical bonding, and the overall crystal structure. Modern software programs have become a vital asset for researchers and materials scientists across multiple disciplines. Using these software programs has proven to be crucial in advancing the understanding of materials and their properties [38].

This study employed two highly specialized and efficient crystallography software: Vesta and CaRIne. Vesta is known for its versatility in crystal structure visualization and analysis, while CaRIne specializes in the analysis of diffuse scattering in crystallography.

### 1.4.1 VESTA, CaRIne crystallography programs

VESTA and CaRIne Crystallography programs are 3D visualization programs for structural, crystal morphologies models, and volumetric data like (nuclear\electron) densities. They also can deal with multiple structural models, crystal morphologies models, and volumetric data at the same window, and they give all information as output files.

VESTA Crystallography Software, which stands for Visualization of Electron/Nuclear and Structures Analysis, is a versatile program mainly used for visualizing and analyzing crystal structures. The software was developed by Professor Koichi Momma and has gained popularity due to its user-friendly interface and robust capabilities. VESTA enables researchers to create, view, and manipulate crystal structures easily. It supports a wide range of crystallographic file formats, making it a versatile tool for crystallographers. In addition to visualization, Vesta provides powerful tools for analyzing crystal structures, including symmetry operations, coordination polyhedral, and electron density maps [39].

CaRIne Crystallography Software is a specialized program designed to analyze diffuse scattering in crystallography. It meets the intricate demands of crystallographers and materials scientists, particularly when it comes to analyzing diffuse scattering in crystal structures. With its specialized capabilities, CaRIne allows researchers to explore and measure structural defects, vacancies, and other irregularities in crystalline materials [40].

It excels in revealing insights into the complexity of disordered materials, making it an invaluable tool for studying glasses, complex oxides, biomaterials, and other substances with non-ideal crystal structures. CaRIne's advanced data fitting algorithms and comprehensive analysis tools give scientists the power to delve deep into the structural intricacies of materials, improving our understanding of their properties and behavior, and facilitating breakthroughs in materials science. To fully understand how materials like AlN respond to irradiation, it's crucial to have a comprehensive understanding of

crystallography. This understanding hinges on the capacity to discern the arrangement of atoms or molecules within the crystal lattice [41].

Crystallography also plays a vital role in identifying the principal axis in AlN crystals. This information is crucial in aligning the ion beam with the crystal axis during RBS/C analysis, which in turn determines the trajectory of the ion beam during experiments.

### 1.5 Simulation software for irradiation and ion beam analysis

Simulation software plays a crucial role in the field of irradiation and ion beam analysis (IBA), as it enables researchers to replicate complex atomic and molecular processes. Simulation software in irradiation and ion beam analysis before and after conducting experiments is preferred due to its ease of use, efficiency, and flexibility.

These techniques simplify complex models into basic events and interactions, making it possible to encode model behavior through a set of rules that can be implemented on a computer with ease. This, in turn, enables researchers to develop and study much more general models on a computer than they could by using analytical methods [42].

Moreover, simulation software algorithms can be highly scalable, which means that the complexity of a simulation program would typically not depend on the number of processes involved. Additionally, many algorithms employed in simulation software can be parallelized, making it possible to run different parts of the program on different computers and processors, thereby reducing the computation time significantly [43].

Through these simulation programs, researchers can obtain a clear initial picture of the results that can be expected after practical experimentation, which saves them a great deal of time, effort, and money.

#### 1.5.1 SRIM simulation

In simulations of a beam of ions hitting a target, variations in the impact parameters of each ion are made to produce different outcomes. The impact parameter is defined as the distance at which particles would pass each other if no forces acted between them. The simulations have an average error of 2%, except for heavy ions in light targets where the error is 5% due to a lack of experimental data to correct the calculations [44].

The Stopping and Range of Ions in Matter (SRIM) software uses the binary collision approximation in its Monte Carlo method, which assumes that the ion moves through the target by experiencing a series of elastic collisions with the atoms in the material. The ion always moves in a straight line and loses its energy to the target electrons through electronic stopping power. The target is assumed to be fully amorphous, and the distance between each collision is equal to $N^{-1/3}$, where N is the atomic density of the material.

A collision integral is evaluated to calculate the scattering angle and energy loss of a binary collision. This collision integral is a complex mathematically constructed equation based on interatomic potentials between the ion and the atom. In a solid target, ions get implanted, and the surface changes during the collision experiment. However, SRIM assumes a target with a fixed composition and does not track such changes.

It is important to note that after multiple approximations, the computation time of SRIM is significantly reduced. However, for accurate analysis, the approximation methods used must be considered [45]. In simulations of a beam of ions hitting a target, variations in the impact parameters of each ion are made to produce different outcomes.

In conclusion, the SRIM package is used for a variety of applications, such as:

1. Calculate the energy loss of ions in matter, which produces tables of stopping powers, range, and range straggling distributions for any ion at any energy in any elemental target. This tool is also used in more complex calculations involving targets with multi-layer configurations.
2. Ion implantation uses ion beams to modify samples by injecting atoms to change the target's chemical and electronic properties. This process also causes damage to solid targets through atom displacement, and the SRIM package contains part of the kinetic effects associated with this kind of interaction.
3. Calculate sputtering, which occurs when the ion beam knocks out target atoms. Any ion can perform this process at any energy. Ion transmission is another application of SRIM, which allows ion beams to be followed through mixed gas/solid target layers, as is the case in ionization chambers or in energy degrader blocks used to reduce ion beam energies [46].

### 1.5.2 RUMP

In 1976, Ziegler and colleagues published the first code capable of performing full Rutherford backscattering (RBS) spectrum simulations, called IBA. In the following decade, several codes emerged, the most popular of which was RUMP. RUMP (Rutherford Universal Manipulation Program) is a software tool designed for RBS (Rutherford Backscattering Spectrometry) plotting, analysis, and simulation. [47]

The RUMP software enables users to plot real RBS random and aligned spectra, as well as user-provided simulation spectra, based on various factors such as energy calibration, composition, and experimental parameters.

These experimental data include the geometry of the detector and the energy of the incident ions. The simulation spectrum depends on the user's entry of the chemical composition, as each chemical element contributes differently to the yield. [48]

This method allows for the identification of the composition that matches the actual spectrum or the chemical composition of the crystal. RUMP helps extract valuable information regarding the elemental composition, depth profiles, and structural characteristics of materials, thus significantly enhancing the efficiency and precision of RBS analysis. This software plays a crucial role in advancing our understanding of atomic-scale properties and contributing significantly to the field of materials characterization [49].

### 1.5.3 Monte-Carlo (McChasy)

The McChasy simulation code, developed at NCBJ Warsaw, is a Monte Carlo code used to simulate the trajectories of ions in a crystal. This helps to calculate the expected ion channeling spectra, assuming a given (defective) structure. McChasy stands for "Monte Carlo Channeling Simulation code". [50]

McChasy is a simulation tool that helps researchers in materials science gain a better understanding of the complex phenomena of ion channeling into crystals. The tool uses the Monte Carlo simulation technique which is specifically tailored for investigating how ion beams interact with crystalline structures. With McChasy, researchers can predict and analyze various outcomes of processes such as radiation damage and structural alterations. The tool can also calculate the backscattering energy spectra obtained at

channeling, random, or any specific angle between the projectile and the normal to the target's surface [50].

McChasy's Monte Carlo method involves the random sampling of probabilistic events such as ion collisions and energy transfers to simulate the behavior of particles over time. Additionally, McChasy is versatile enough to simulate complex depth distribution of defects and their nature, making it an indispensable tool for researchers who seek a deep and nuanced understanding of material behavior through computational modeling. The provided code presupposes a specified crystal structure and permits the incorporation of various structural defects. These defects include the amorphization of a fraction of matrix atoms within a designated sublattice, termed randomly displaced atoms, and dislocations characterized by size and density. The concentrations of structural defects can be specified at any depth. Comparing the calculated spectra with experimental data allows the extraction of pertinent information regarding the distribution of defects in the actual crystal [51].

Defining several parameters in the initial stage is crucial for accurate results. These parameters encompass crystallographic structure, composition, experimental geometry input/output angles, characteristics or parameters of the incident beam, and detector parameters. In Monte Carlo simulations, the crystal is divided into several layers with increasing depth. A random initial impact parameter ($p_0$) is selected from a uniform distribution, and changes to it are then calculated. The simulation uses a Coulomb-screened potential to model interactions between ions and atoms, which determines the path of the incoming particle. It is important to mention that McChasy consistently employs a single crystal cell, apart from an initial random selection of the impact parameter [52].

The Monte Carlo simulation method offers a significant advantage as it enables a quantitative examination of crystals with a range of authentic defects, unlike traditional dechanneling studies that rely on simplified defect models and analytical analysis of experimental spectra.

## 1.6 Objectives of the Study

The aim of this thesis is to investigate the influence of helium on the microstructure of aluminum nitride (AlN) single crystals, focusing on the helium concentration and ion implantation temperature. The damage will be characterized using Rutherford Backscattering Spectrometry in Channelling geometry (RBS\C) technique.

The effect of helium presence in AlN will be explored using single crystalline layers of AlN deposited on a substrate as a model system. These crystals will be bombarded with energetic He ions at the JANNuS-Orsay experimental hall located at the MOSAIC facility, IJCLab, to simulate helium presence.

The He-implanted single crystals will be characterized using ion channeling of light ions and Rutherford backscattering spectrometry to extract the depth distribution of displaced solid atoms and monitor structural transformations, such as material amorphization at large fluence. Monte Carlo simulation code will be utilized for a full analysis of experimental spectra to quantify radiation effects as a function of bombarding particle fluence.

Various models of radiation-induced defects will be tested to simulate experimental ion channeling spectra and achieve a comprehensive description of crystal evolution from lightly damaged to the highest envisaged irradiation fluences expected in a fusion system.

These steps will be taken to propose a model of crystalline defects creation in AlN and its healing rates based on sample chemistry, temperature, and to determine the viability of AlN as a nuclear material in a nuclear reactor.

The results obtained in this internship will be used to complete those obtained during Gabriel Bouhali's Ph.D. thesis (ED PHENIICS, IJCLab, defense on 21$^{st}$ December 2023).

# Chapter Two

# Experimental Work: Materials and methods

All of the experimental work in this master thesis was performed within the CHIMèNE team (Chemistry, Irradiation, Materials, Modeling, and Electrochemistry for Nuclear Energy), and in particular the Material and irradiation theme, at the Energy & Environment pole at IJCLab, the Laboratory of the 2 Infinities Irène Joliot-Curie, located on the Orsay campus, France. Some of the equipment of the MOSAIC ion beam facility was used, in particular the ARAMIS ion accelerator located in the JANNuS-Orsay experimental hall [53].

AlN crystals were prepared, implanted, and irradiated with ions to make the crystals ready before the first characterization by Rutherford Backscattering Spectrometry in Channelling Geometry (RBS/C) and other analysis methods.

## 2.1 Sample preparation and Ion implantation irradiation (as-received condition)

The aluminum nitride (AlN) sample preparation process consists of many steps including:

- Starting with synthesizing the crystal. An AlN epitaxial film with a thickness of 4μm was deposited on a substrate with a thickness of 300μm, composed of $Al_2O_3$ Ceramic Substrate (ADS-996) and grown by MTi, which was previously purchased [54]. (MTi: name of the substrate company which used to grow the samples on it).
- The second step was crystal cutting, as the as-received wafer was typically a 10 cm diameter circle, while only a roughly 1 $cm^2$ specimen was required for damage characterization under a single irradiation condition. Since AlN was a tough crystal, the machine used for this step featured a diamond edge.
- The next step was cleaning: after cutting, it was necessary to remove all dust and any material layers adsorbed on the surface of the sample by cleaning the pieces in an acetone and ethanol bath (as described in 2.4).
- The final step was the deposition of a thin carbon layer on the surface, mandatory for ion beam analysis of insulating materials (see details in paragraph 2.4), to avoid charge effects due to the insulating material.

The as-received samples are then ready for as-received characterization using ion beam analysis (and more specifically RBS/C, see its principle in paragraph 2.5), and for ion irradiation.

The ion implantation in this experiment has been performed using a 190 kV IRMA ion implanter and/or the 2MV ARAMIS ion accelerator. IRMA and ARAMIS are two of the 4 ion beam accelerators of the MOSAIC facility, located in the JANNuS-Orsay experimental hall, the other ones are SIDONIE and Andromède.

ARAMIS is an ion accelerator with a nominal voltage of 2 MV, which was developed in the laboratory in the 80s. Equipped with various sample holders, the ARAMIS ion accelerator allows a wide range of ion irradiation and material synthesis analysis studies to be carried out.

Thirty five chemical elements are available from one of the two ARAMIS ion sources (a positive source (Penning type) and a negative source (Middleton)) and make it possible to carry out ion beam analysis and ion implantation and "self-irradiation" damage studies (including "self-irradiation", without adding chemical pollution, i.e. choosing an element already present in the specimen to be irradiated), with fluxes between $1\times10^{9}$ and $1\times10^{12}$ at/(s.cm$^{2}$) [53]. The irradiation temperature can vary from -170°C to 1000°C, as seen in Figure 2.1.

The IRMA ion implanter can deliver ion beams of 65 different chemical elements, with energies ranging from 5 to 570 keV, allowing materials to be modified up to 500 nm in depth.

The three ion beam accelerators have different features (for example ARAMIS has both a positive source (Penning type) and a negative source (Middleton). In contrast, the two others have only a positive source), different ranges of energy, and different usages and operating temperatures of -170 - 1000$^{o}$ C.

**Figure 2.1**

*Sample preparation and Ion implantation irradiation (as-received condition)*

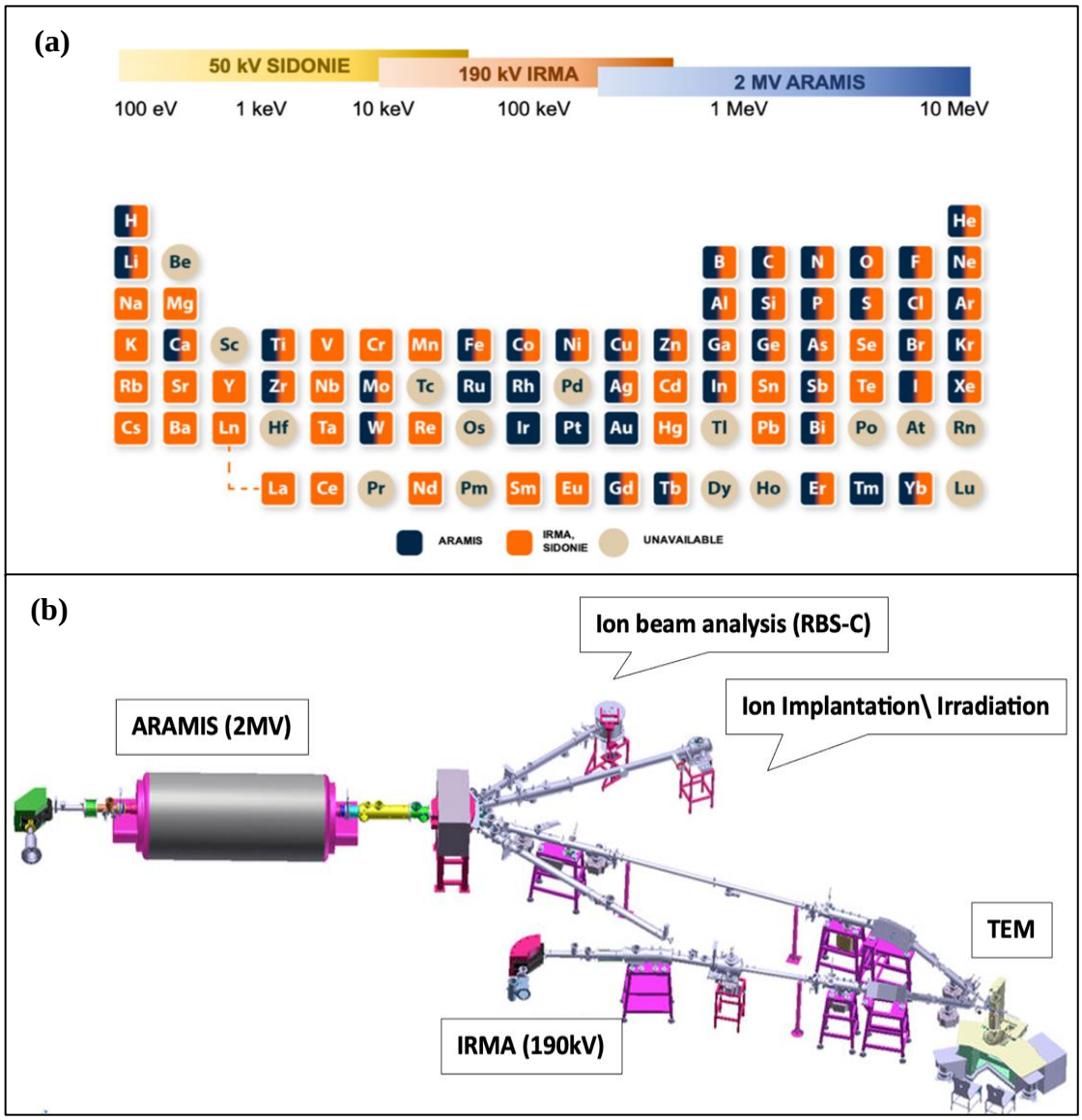


Note: (a) Operating energy range and elements available to accelerate as an ion beam in ARAMIS, IRMA, and SIDONIE accelerators. (b) Overview of the JANNuS-Orsay experimental hall/MOSAIC platform. Ishikawa, et al. (2000).

The accelerators ARAMIS and IRMA are connected, and there are 5 beamlines in the hall. One of these lines is for Ion Beam Analysis (IBA), which is used for the structural and chemical characterization of materials using Rutherford Backscattering Spectrometry (RBS, RBS/C), Particle-Induced X-ray Emission (PIXE), and Elastic Recoil Detection Analysis (ERDA). Two beamlines are custom to the ion implantation/irradiation process, and the last two lines are employed for connecting the accelerators IRMA and ARAMIS to a Transmission Electron Microscope (TEM), allowing in situ observation at the

nanoscale of modifications induced in a material by ion irradiation with one or two ion beams.

6 samples of AlN were irradiated with different fluences (number of ions/cm2) with a beam of $Au^+$ ions at an energy of 6 MeV.

Irradiations were performed at room temperature (RT) to fluences between ($3.1*10^{14}$ $cm^{-2}$, and $4*10^{15}$ $cm^2$), One sample was kept virgin (without ion irradiation, in the as-received state), as shown in Table 2.1. Ion irradiations were performed at 7° off the (0001) surface.

**Table 2.1**

*Implantation fluences were used to implant the crystals with 6MeV $Au^+$ ions at room temperature*

| Sample | Fluence ($cm^{-2}$) |
|---|---|
| $\varphi_{0\ (virgin)}$ | 0 |
| $\varphi_1$ | $3.1x10^{14}$ |
| $\varphi_2$ | $7x10^{14}$ |
| $\varphi_3$ | $1.5x10^{15}$ |
| $\varphi_4$ | $2.2x10^{15}$ |
| $\varphi_5$ | $3.0x10^{15}$ |
| $\varphi_6$ | $4.0x10^{15}$ |

## 2.2 SRIM simulation

Before the experiment, the SRIM simulation program was utilized to gain a more accurate understanding of the ion implantation/irradiation process (the deposition of ions into a target material). SRIM simulations provide predictions of ion behavior as they penetrate the material, calculating ion ranges (depth), energy distributions, and damage profiles. These predictions are essential for understanding and controlling the ion implantation process prior to conducting RBS-C analysis.

For this study, SRIM simulations were performed on the AlN crystal under the same conditions used in the irradiation process. This included a 7° angle offset relative to the ion beam, nearly perpendicular to the specimen surface. The simulations were conducted for $Au^+$ ions with an energy of 6 MeV, as well as other ions (He ions at 50 keV and Al ions at 280 keV) to compare the damage profiles in AlN crystals resulting from different ion types and energies. See Figure 2.2 for details.

**Figure 2.2**

*Depth profiles of implanted ions with different energies in the AlN target at a 7° angle using the SRIM simulation program*

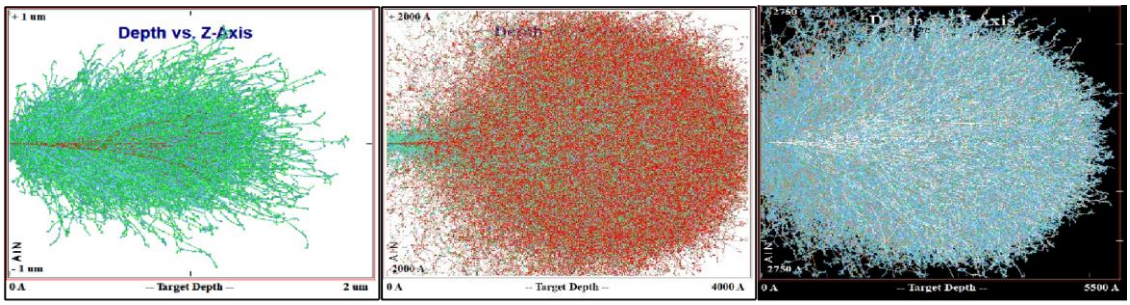


Note: (a) 6MeV Au+ ion beam (b) He (50keV) ion beam (c) Al (280 keV) ion beam.

After the simulation was done, the number of displacements per atom (dpa), and the concentration of implanted ions in the target crystal were calculated by using equations 2 and 3 based on the simulation results.

The number of displacements per atom (dpa) (used to measure the damage in an irradiated material), was calculated by using equation 4:

$$\text{dpa} = N_{\text{displaced atoms}}/N_{\text{total atoms}} = (N_{\text{displ. atom}}/V)/(N_{\text{total. atom}}/V) \quad (4)$$

$$\text{where } (N_{\text{displ. atom}}/V) = (N_{\text{displ. atom}}/\phi)/\Delta x$$

$$= \frac{\left[\frac{N_{\text{displ.stom}}}{\Delta x}\right]^{\text{SRIM}} \left[\frac{N_{ions}}{S}\right]}{\left[\frac{N}{V}\right]_{\text{atom}}}$$

$$\text{so dpa} = \frac{\left[\frac{N_{\text{displ.stom}}}{\Delta x}\right]^{\text{SRIM}} \Phi_{ions}}{\left[\frac{N}{V}\right]_{\text{atom}}}$$

With:

$N_{\text{displaced atoms}}$: number of displaced atoms

$N_{\text{total atoms}}$: number of total atoms

V: volume ($cm^3$)

$\phi$: the fluence ($at.cm^{-2}$)

$\Delta x$: target depth (Ang.)

S: irradiated area of the layer

The impurity fraction that was incorporated into the material during the ion implantation/irradiation process was calculated by using Equation 5:

$$\text{Impurity Fraction} = \left( \frac{(N/V)_{\text{impurities}}}{(N/V)_{\text{target material}}} \right) \times 100\% \quad (5)$$

This can also be expressed as:

$$\text{Impurity Fraction} = \left( \frac{(N/V)}{(N/S)} \times \phi \right) /(N/V) \times 100\% \quad (6)$$

Where:

N/V: represents the number density per unit volume.

N/S: represents the number density per unit surface area.

$\phi$: is the related factor for impurities.(at.cm$^{-2}$)

All results of these simulations will be discussed in Chapter 3.

### 2.3 Crystallography of AlN

As mentioned in the introduction, defects are a common occurrence in both natural and industrial crystals, as perfect crystals don't exist. When crystals are exposed to ion beam irradiation, there is an increase in displaced crystal atoms, resulting in the formation of Frenkel pairs defect. This displacement can alter the positions of atoms, causing damage to the crystallographic lattice, affecting specific orientations, or even leading to amorphization. Understanding the crystallography of a material, such as AlN in this study, is crucial for predicting its response to irradiation. It allows us to determine the arrangement of atoms or molecules within the crystal lattice, providing insights into its behavior under irradiation.

Crystallography also helps to know what the main axis in the AlN crystal is, which is important for aligning this main axis with the ion beam used during RBS/C analysis, thus choosing the path that the ion beam will follow during RBS-C ion beam analysis experiments. There are two different paths used by the ion beam in our RBS-C analysis of AlN single crystals: one is aligned along the c-axis of the crystal, and the other one is random. In an aligned ion beam, the line axis's orientation or the beam's channels will be known. In the random path, the orientation of the crystal keeps changing randomly so it

can get the maximum yield of backscattered atoms because the ion beam will collide with a high number of displaced atoms in the crystal.

The hexagonal AlN crystal, belonging to the $P6_3mc$ space group, with dimensions {a = b = 313 pm, c = 502 pm} and angles {$\alpha = \beta = 90°$, $\gamma = 120°$}, was modeled using the Vesta crystallography software program [32]. This process included determining the four principal axes: $a_1$ [2-10], $a_2$ [-120], $a_3$ [-1-10], and c [001]. The results of this analysis are presented in Scheme 2.1.

**Scheme 2.1**

*Crystallography of AlN*

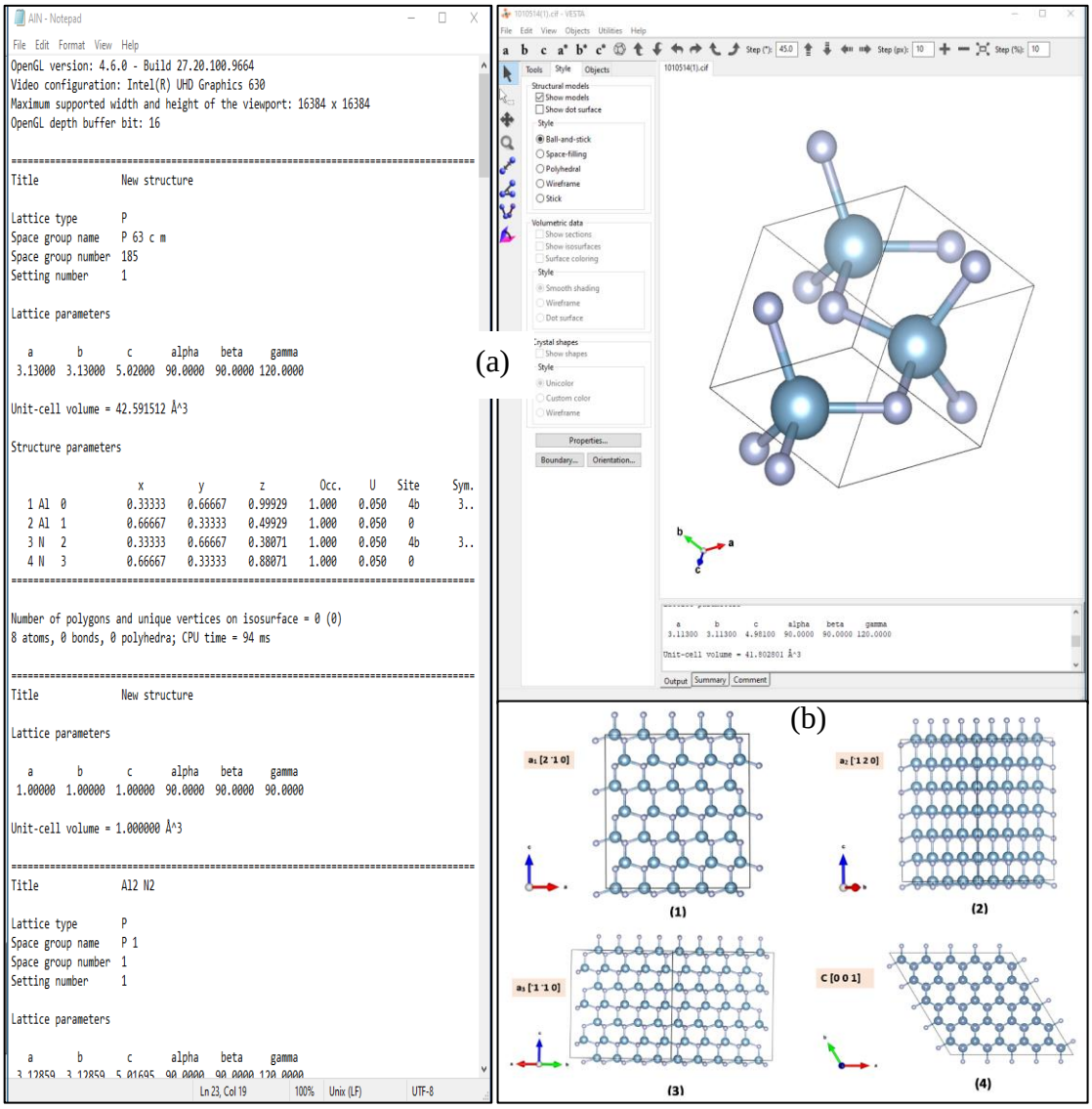


Note: (a) Example of an input file from Vesta crystallography software program to draw the hexagonal AlN crystal (b) The main four axes in the crystallographic structure of AlN crystal (1) $a_1$ [2 ¯1 0] (2) $a_2$ [ ¯1 2 0] (3) $a_3$ [¯1 ¯1 0] (4) c [0 0 1].

## 2.4 Carbon layer deposition

The final step in preparing the AlN crystal for RBS-C analysis involved depositing a graphite layer onto the polished surface of the samples. This step, which adds a conductive carbon layer, was crucial to prevent surface charge effects (charge accumulation) during the RBS characterization, ensuring accurate and reliable analysis. Without the carbon layer, the He ions used in RBS analysis would accumulate on the crystal's surface due to the insulating nature of AlN. This charge buildup would distort the RBS spectrum, rendering it unanalyzable.

Prior to depositing the carbon layer, all samples were thoroughly cleaned using acetone ($CH_3COCH_3$) followed by ethanol ($C_2H_5OH$) to ensure the removal of any surface impurities. The AlN crystal features two distinct sides: the polished (shiny) side, corresponding to the AlN layer, and the substrate side. The carbon deposition was specifically carried out on the polished AlN side. The carbon deposition process was carried out in multiple steps. In each step, by using carbon rods a very thin carbon layer was deposited sequentially onto the surfaces of six samples in the following thicknesses: 0.4 nm, 0.8 nm, 0.4 nm, 0.4 nm, 0.8 nm, 0.4 nm, 0.8 nm, 0.4 nm, 0.4 nm, 0.4 nm, and 1.2 nm. This process resulted in a total carbon layer thickness of 6.4 nm.

The deposit process was done using a carbon coater machine (Cressington carbon coater), see Figure 2.3 (a). The carbon coater machine was coupled to a pump responsible for providing a vacuum inside the system. Electric current was then passed through a thin graphite wire resulting in its evaporation and deposition to the samples located below it.

With the carbon conductivity, no electric charge accumulates at the crystal surface and $He^+$ ions used during the RBS/C analysis can then penetrate inside the crystal and be backscattered to the detector providing reliable elastic backscattering spectra. After finishing the previous process, all samples were fixed on a metallic holder one by one in a specific order using carbon tape in a specific order (see Figure 2.3 (b)).

**Figure 2.3**

*Carbon layer deposition*

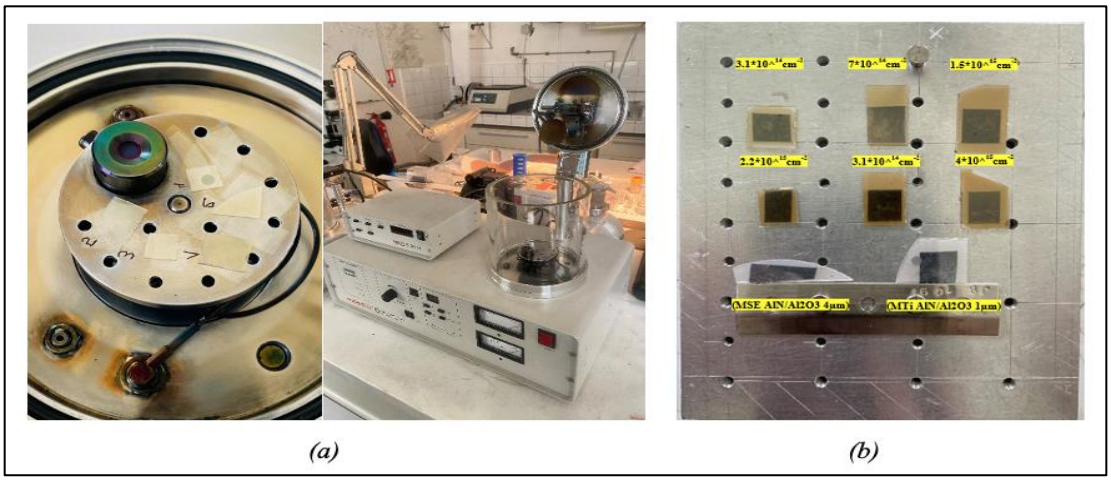


Note: (a) A carbon coater machine (Cressington carbon coater) is used to deposit a graphite layer on the face-polished crystals (b) The aluminum holder containing the samples is fixed by using carbon tape.

## 2.5 Rutherford Backscattering Spectrometry (RBS-C) experiment

Rutherford Backscattering Spectrometry in Channeling geometry (RBS-C) is a highly effective tool for analyzing the damage caused by He+ ion irradiation in AlN crystals. When energetic ions such as He+ collide with a crystal lattice, they can displace atoms from their regular positions, create vacancies, and induce structural defects.

RBS-C can precisely determine the extent and nature of this damage by measuring the backscattered incident helium ion's energy and angles. By comparing the spectra before and after 6 MeV $Au^{+}$ ion bombardment, the information about the density of defects, such as vacancies or interstitials, as well as their distribution within the crystal lattice, can be determined. RBS-C analysis is crucial for understanding the response of materials to radiation or ion implantation, aiding in the development of radiation-resistant materials, and advancing applications in semiconductor manufacturing and nuclear materials research.

In this experiment, RBS-C was performed using helium ions delivered by the ARAMIS accelerator in the JANNuS-Orsay. The beamline used to experiment is equipped with a suitable sample holder (made of aluminum) to hold the samples at a correct angle and a holder to fix the detector at a suitable angle as well. The scattering angle was constant at 15°.

The sample holder is remotely movable for the beam to cover all the samples. The characterization beam uses $He^+$ 1.5 MeV as kinetic energy, this value of the energy was selected since it allows a good separation of the various chemical elements of the AlN crystal while keeping a good depth resolution that allows the depth distribution of defects to be extracted by channeling with good precision.

Before starting the analysis, an alignment procedure of the goniometer was made to align the ion beam direction with the main axis [c axis 0001] for all of the AlN samples.

Furthermore, adjustments were carried out in both the horizontal (x) and vertical (y) directions to ensure that the beam fully struck the crystal without any portion of it hitting the holder, this confirmation was achieved by capturing RBS yield spectra while operating the goniometer in random mode, involving continuous rotation (within a 4-degree cone) relative to the major crystal axis. If the spectrum presents a characteristic front for the various atoms that constitute AlN and does not present the aluminum signal of the holder, then the beam is said to be impinging on the sample, this can be confirmed by recording spectra at multiple positions along the crystal, spanning from one end to the other.

The primary c-axis for ion channeling was determined by carrying out angular displacements in the rotation angle (α) around the y-axis, and rotation angle (β) around the x-axis of the goniometer. This process aimed to identify specific (α, β) coordinates to exhibit the lowest backscattering yields. The dose (charge) was systematically varied at regular intervals to enhance the statistical data collection for the AlN crystal. The current was adjusted automatically to maintain a constant ion beam fluence.

The first RBS-C spectra showed that there is a charge effect in the AlN samples, this charging effect appeared because the carbon layer was not thick enough to prevent it.

An extra 7 nm of carbon was deposited on each AlN sample, and the total carbon layer thickness for the 6 samples was 13.4nm, as a precaution all carbon tape used to fix the sample was removed by dissolving it with alcohol (acetone\ methanol), and instead of carbon tape, metallic pieces were used to fix the samples. The final RBS-C spectra were collected with no charge effect in the AlN samples.

All recorded RBS-C spectra (random and aligned) which show the various fronts corresponding to the various chemical elements, will be discussed in section 3.2 in Chapter Three.

## 2.6 Analysis of the RBS-C experimental spectra

The interpretation of experimental spectra generated by the RBS-C experiment is a crucial and intricate process that enables us to gain insights into the composition and structure of materials, as well as the damage sustained by the AlN crystal. To extract useful information from the data collected, by using McChasy code and RUMP software.

### 2.6.1 RUMP simulation

The Rutherford Universal Manipulation Program (RUMP) is a sophisticated tool that streamlines RBS plotting, analysis, and simulation. It empowers users to create authentic RBS random and aligned spectra and simulate spectra by adjusting factors like energy calibration, composition, and experimental parameters that are needed for subsequent McChasy simulations. The simulated spectrum is influenced by the chemical composition the user provides, as each element uniquely impacts the yield.

The first step in this analysis is writing a code that will be run by RUMP software to graph the experimental data obtained through (RBS) for all of the AlN samples, as shown in Figure 2.4. This process involves considering a range of parameters, including the energy of the incident particles, the composition of the target material, and the scattering angles, to construct a model that accurately represents the interaction between the incident particles and the target material.

The composition and thickness of the layers formed were determined by simulating the experimental spectra RBS obtained by the RUMP software with standard experimental conditions, particle beam $He^{+}$, 1.5 MeV energy, at an angle of detection of 165°.

All results of these simulations are shown and discussed in Chapter 3.

**Figure 2.4**

*RUMP simulation*


Note: Figure (a) (b) describes the codes employed by RUMP software to graph the experimental data obtained through the (RBS) technique for all samples of (AlN).

### 2.6.2 McChasy simulation

McChasy (abbreviation for Monte-Carlo CHAnnelling SImulation) is a technique that uses computational methods to replicate the movement of ions in crystals. This enables the creation of simulated Rutherford Backscattering Spectroscopy (RBS) spectra that can be compared with experimental data. The development of this method was based on the groundbreaking work of Barrett.

The simulations involve computing ion trajectories through a series of iterations. At each iteration, the deflection of ions is determined, taking into account factors such as the screened Coulomb potential (the Coulomb potential describes the electrostatic interaction between ions and atomic nuclei or electrons. The screened Coulomb potential accounts for electron cloud effects, reducing the force at longer distances and enabling accurate modeling of ion deflection in the crystal lattice), thermal vibrations of atoms, and energy loss within a specific depth interval in the crystal. The normalized nuclear encounter probability (NEP) is then determined and used in the simulation process. The McChasy code was used to analyze the experimental RBS/C spectra in this study. The McChasy code simulates the trajectory of light ions ($He^+$) traveling through AlN crystals; the code performs efficiently when dealing with heterostructures, superlattices, and materials that contain complex defects. The software also employs independent depth profiles of various defect types, such as interstitials, edge dislocations, substitutions, stacking faults, and grain boundaries to provide a fitting procedure for RBS/C spectra. The fitting procedure generates calculated channeling spectra as output that can be used to facilitate further analysis of the sample's structural properties [51].

The McChasy code's simulation outputs were observed to be in excellent alignment with the recorded spectra. The McChasy program follows a three-step process to conduct its analysis. The initial step in the McChasy simulation process involves the creation of an input file and this input file continues all experimental data, including ion beam characteristics, target characteristics, experiment geometry, crystal structure, chemical composition, thermal vibration, the solid angle of detector, incident and backscattering angle, nature of analyzing ion, energy, beam divergence, and energy resolution were inputted as a file into the code. For each $Au^+$ fluence, which corresponds to a different RBS/C spectrum, the fraction of radiation-induced defects at a given depth (RDA) was set as input in the MC simulation. Next, the crystal is divided into thin layers and the

McChasy simulation provides an estimate of the concentration of the defects for each layer. The McChasy code employs a formula based on Monte Carlo ion trajectory simulation methods, emphasizing interaction probabilities between ions and the crystal lattice.

While the exact formula is not detailed in the paragraph, the process relies on key principles such as:

- Screened Coulomb potential for ion-atom interactions. A typical formula for the interaction might be:

Here:

$$V(r) = \frac{Z_1 Z_2 e^2}{4\pi\epsilon_0 r} \cdot \phi(r/a) \quad \textbf{(7)}$$

Z1 and Z2: Atomic numbers of the ion and target atom.

e: Elementary charge.

$\epsilon 0$: Vacuum permittivity.

r: Distance between the interacting particles.

$\phi(r/a)$): Screening function, with aa being the screening length.

- Nuclear and electronic stopping powers, which describe energy loss by the ions:

$$S = S_n + S_e \quad (8)$$

Where:

Sn: Nuclear stopping power (collisions with nuclei).

Se: Electronic stopping power (energy loss to electrons).

- Radiation Defect Accumulation (RDA): The input fraction of radiation-induced defects is likely modeled using depth-dependent probability distributions to estimate defect concentrations in each crystal layer. This is often linked to nuclear stopping interactions.

The simulation is then run, producing a channeling spectrum that details the backscattering events at each acquisition channel, and the calculated and experimental spectra are compared. If necessary, the defect concentration can be adjusted to improve the fit. This updated input file is used to rerun the simulation code, and the process repeats until an optimal fit is achieved. Finally, the acquired spectra are normalized to enable comparison with experimental data.

The simulation is a time-consuming and labor-intensive process demanding proficiency and self-assessment. It involves numerous runs of systematically adjusting the depth distribution of defects to achieve a resemblance to the experimental spectrum.

The progression of the damage-depth distribution with ion fluence is obtained and scrutinized. Table 2.2 illustrates an example of a typical input file used in the study, where the data helps determine the optimal depth distribution of RDA defects that closely replicates the experimentally captured aligned spectra.

**Table 2.2**

*Example of an input file from McChasy code for different RDAs that were used*

```
PAR 50000
PRO helium      Projectile
ENE 1496        Projectile energy in keV
ESP on
IBD 0.12        Ion beam divergence in deg
SCA 165         Scattering angle in deg
ANG 0  15       Input and exit angles in deg
OMC 3.3 0.0622  Solid angle (msrad) and charge (microC)
RES 22          RBS energy resolution in keV
BEC 4.741  32.935   Width of RBS energy channel in keV and offset
TGT AlN         Name of the structure
KLM 001         Channeling axis
THI  1500       Range of simulation
VIB Al   5      1..D thermal vibrations in pm
VIB N   10
ESC on
FOR rump        Electronic stopping uses the rump approximation
LEL 2           local fraction of energy loss, 2 layers
*** depth( nm ) value   obligatory comment
 1 0     0.5
 2 2000  0.5
***
***             ele         f           step            No
RDA             all         1           step            58
***             depth       weight
1               0           0
2               5           0
3               10          0.1
4               15          0.1
5               20          0.1
6               25          0.1
7               30          0.1
8               35          0.1
9               40          0.1
10              50          0.2
11              55          0.4
12              60          0.6
13              70          0.8
14              80          1
15              90          1.2
16              100         1.3
17              110         1.4
18              150         1.5
19              170         1.6
20              190         1.7
21              200         1.8
22              230         1.9
23              250         2
24              280         2.2
25              300         2.4
26              310         2.6
27              320         2.8
28              350         3
29              380         3.2
30              400         3.4
31              430         3.6
32              450         3.8
33              480         4
34              500         4.5
35              520         5
36              550         5.5
37              570         5.75
38              590         6
39              620         6.5
40              640         6.75
41              650         7.25
42              660         7.5
43              670         7.75
44              680         8
45              700         8.25
46              720         8.5
47              750         8.75
48              780         9
49              800         9.25
50              820         9.5
51              850         9.75
52              900         10
53              920         10.2
54              950         10.4
55              970         10.6
56              1000        10.8
57              1100        12
58              1500        25
DWI 1   100  200
DWI 2   100  500
GON scan 13
TET 1
1   0.0
EXE a
GON rotate 4
EXE b
AMO  on
GON static 0 0
EXE c
```

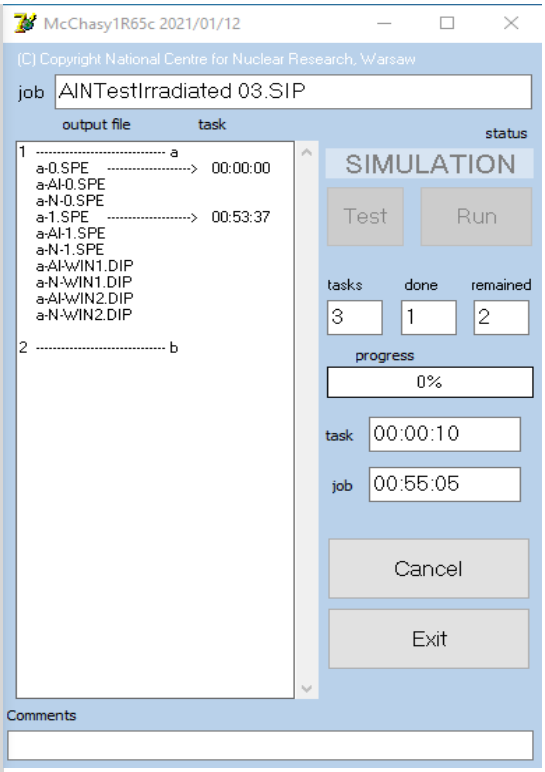


Note: *The first column at left is a command to the code corresponding to a parameter to be fixed followed by its name or by its value (in this example PRO helium is the He probing ion and ENE 1496 its energy in keV)*

# Chapter Three

# Results and Discussion

## 3.1 SRIM simulation results: depth profiles, impurity fraction (at%), and damage (dpa)

A calculation using SRIM was performed to estimate the stopping and range of various projectiles in an AlN crystal. The SRIM data was also used to determine the damage distribution in the crystal after simulated implantation with 6MeV $Au^{+}$ ion, by drawing a graph showing the total number of vacancies in the crystal as a function of depth (measured in nanometers), depth profiles refer to the distribution of implanted ions, impurities, or damage as a function of depth within the target material.

These profiles provide insight into how ions penetrate and interact with the material, showing how far the ions travel, their concentration at various depths, and where they primarily accumulate or cause structural modifications.

Scheme 3.1 shows that at the maximum fluence for 6MeV Au at a depth of 860.001nm, the maximum number of total vacancies (maximum damage) is 2.08 . As a result, it can be observed that there are different interactions between ions and AlN crystals depending on ion mass and energy, for example, the point of using 6MeV Au is to create a large cascade of damage by using heavy elements, as observed from Scheme 3.1

When ions are implanted into materials, they create damage by transferring energy to the orbital electrons and nuclei that make up the material. As the ions travel through the material, they lose energy, which causes changes and damage to the material. The amount of energy transferred is not constant and depends on collisions. This transfer of energy depends on factors such as the nature and initial energy of the ion, as well as the constituents of the material it passes through. [42][54]

**Scheme 3.1**

*The damage distributions (at the maximum fluence) for each of (a) 6MeV $Au^+$, (b) 50 keV $He^+$ ion, and (c) 280 keV Al ion, were calculated according to the SRIM code*

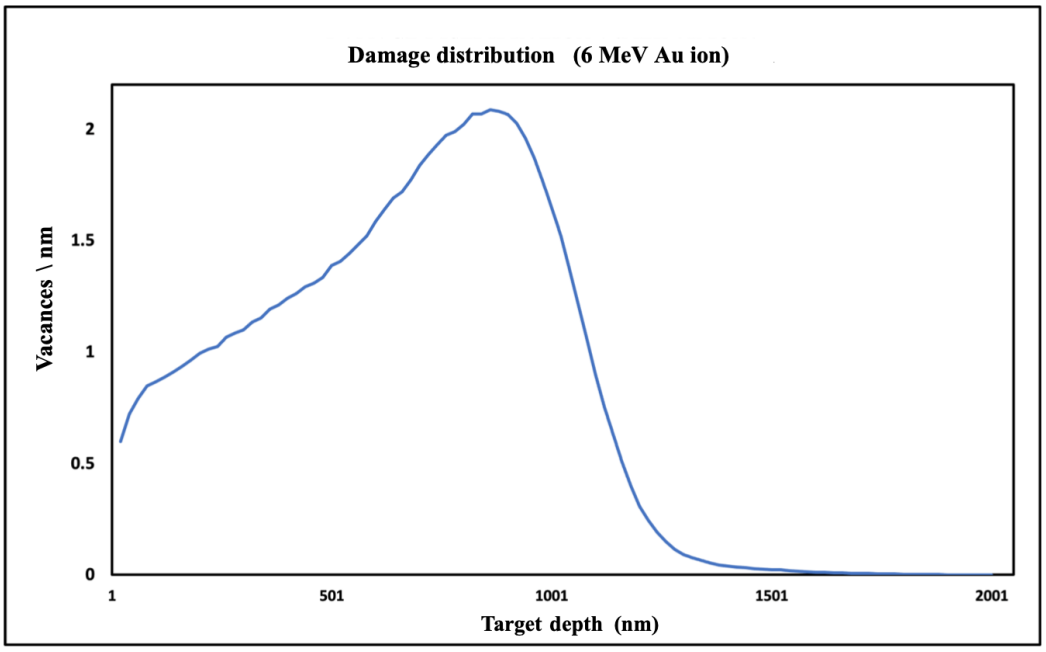


The results obtained from Figure 3.1 were used to calculate the number of displacements per atom (dpa) for $Au^+$ ions induced during the irradiation using Equation 4, as shown in Table 3.1.

Theoretically, the material damage is directly related to the displacements per atom (dpa) via the residual defects from induced displacements. However, in practice, the material damage is based on a correlation to the high-energy (E > 1.0 MeV) neutron fluence.

Where dpa as mentioned before, stands for Displacements Per Atom, is a standard parameter used to determine the amount of radiation damage in materials. It is an important measure that takes into account both the material response (displaced atoms) and the magnitude and spectrum of the neutron fluence to which the material was exposed. dpa is a useful metric for comparing the radiation effects of low-energy ions under different conditions. The dpa can vary depending on the ion's mass and energy.

As seen in Table 3.1 the relationship between fluence and the dpa is a direct correlation and a proportional relationship.

**Table 3.1**

*The number of displacements per atom (dpa), which were calculated using Equation 4 by using different fluence of $Au^+$ ions.*

| Fluence ($cm^{-2}$) | dpa |
|---|---|
| $3.1x10^{14}$ | 0.7 |
| $7x10^{14}$ | 1.5 |
| $1.5x10^{15}$ | 3.3 |
| $2.2x10^{15}$ | 4.8 |
| $3x10^{15}$ | 6.5 |
| $4x10^{15}$ | 8.7 |

Also, the ion range for $Au^+$ ion was determined by using SRIM simulation data as seen in Scheme 3.2

**Scheme 3.2**

*The Ion range (at the maximum fluence ($4x10^{15}$)) for 6MeV $Au^+$*

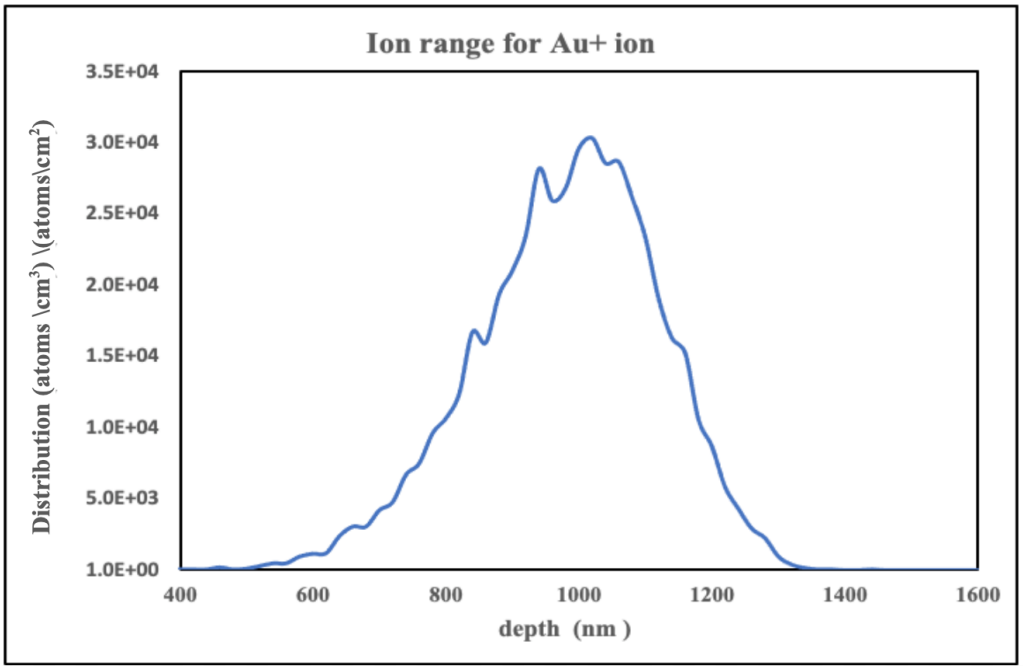


By using data from Scheme 3.2 the impurity fraction that was incorporated into the material during the ion implantation/irradiation process was calculated using Equation 5

**Table 3.2**

*The impurity fraction at 100%, which was calculated using Equation 5 by using different fluence of $Au^+$ ions*

| Fluence ($cm^{-2}$) | impurity fraction at 100% |
|---|---|
| $3.1x10^{14}$ | 0.01 |
| $7x10^{14}$ | 0.02 |
| $1.5x10^{15}$ | 0.05 |
| $2.2x10^{15}$ | 0.07 |
| $3x10^{15}$ | 0.09 |
| $4x10^{15}$ | 0.13 |

Table 3.1 shows a direct and proportional correlation between fluence and impurity fraction.

### 3.2 Data analysis of the RBS-C spectra

To thoroughly examine the elemental composition, depth profile, and defect formation within AlN crystals implanted with $Au^+$, RBS-C spectra analysis is required. As mentioned before, when $Au^+$ ions are implanted into AlN crystals, they can cause defects like vacancies, interstitials, and lattice distortions due to differences in atomic size and lattice parameters between Au and AlN [55].

To analyze the implanted AlN crystal's RBS-C spectra data, RAMP and Monte Carlo simulation techniques and ion range calculations were used. By comparing the RBS spectra of the AlN crystal with a simulated one of $Au^+$ implanted crystals, characteristic peaks or shifts that indicate the presence of $Au^+$ ions and the induced defects can be identified.

At room temperature and by using (1.5 MeV) $He^+$ as a characterization beam, AlN crystals underwent RBS/C experiments. Scheme 3.3 shows the RBS-C aligned and random spectra recorded for all implanted AlN samples were extracted and plotted from the data collected with RBS-C. The comparison of the various random spectra recorded for the different samples shows that there is a difference observed pre- and post-

implantation. Such a result was predictable because $Au^+$ is a heavy element so it can substantially impact RBS signals in random and aligned directions [56].

The spectrum recorded on the virgin sample displays a favorable channeling behavior, with minimal axial yield and a low number of native defects in the crystal. However, as the ion fluence increases, we observe the emergence of a growing peak indicating damage in all sublattices.

**Scheme 3.3**

*RBS/C aligned (A) and random (R) spectra were recorded for implanted AlN crystals at room temperature with the 6MeV $Au^+$ ion at various ion influences*

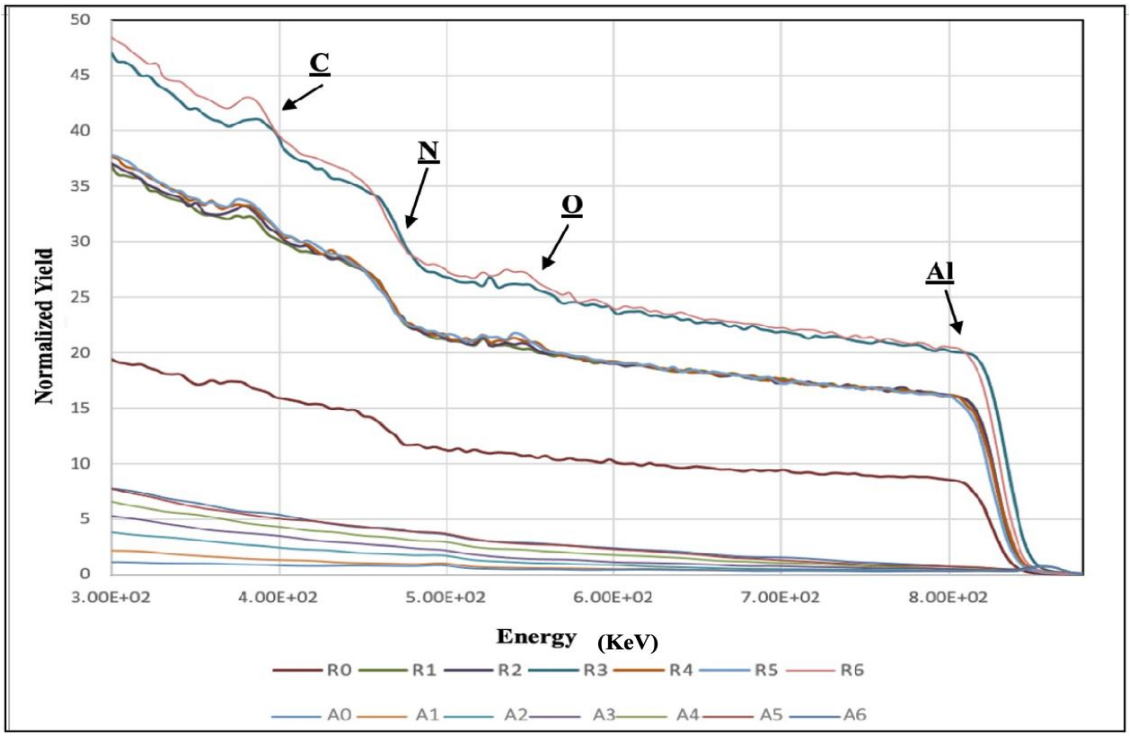


The various elements present in the AlN crystal concerning its depth were determined by using kinematic factor {equations (2) and (3)}, so by using the previous equations the peak for aluminum is located at (834 KeV), nitrogen (478 KeV), carbon (389 KeV) from carbon layer deposition, oxygen (550 KeV) appears because amount of oxygen accumulated in the surface of AlN crystals during carbon deposition process, as shown in Scheme 3.3.

To compare experimental and simulated data, all simulations were conducted at room temperature using the McChasy code. The code was applied to simulate the number of

defects caused by $He^+$ irradiation by modeling the disorder using RBS spectra recorded. Scheme 3.4 displays the MC fits of the experimental RBS spectra at increasing fluences: $\varphi_0 = 0$, $\varphi_1 = 3.1x10^{14}$, $\varphi_2 = 7x10^{14}$, $\varphi_3 = 1.5x10^{15}$, $\varphi_4 = 2.2x10^{15}$, $\varphi_5 = 3x10^{15}$, $\varphi_6 = 4x10^{15}$

**Scheme 3.4**

*Monte Carlo simulation of RBS/C spectra of AlN crystals irradiated with 1.5 keV He ions at room temperature*

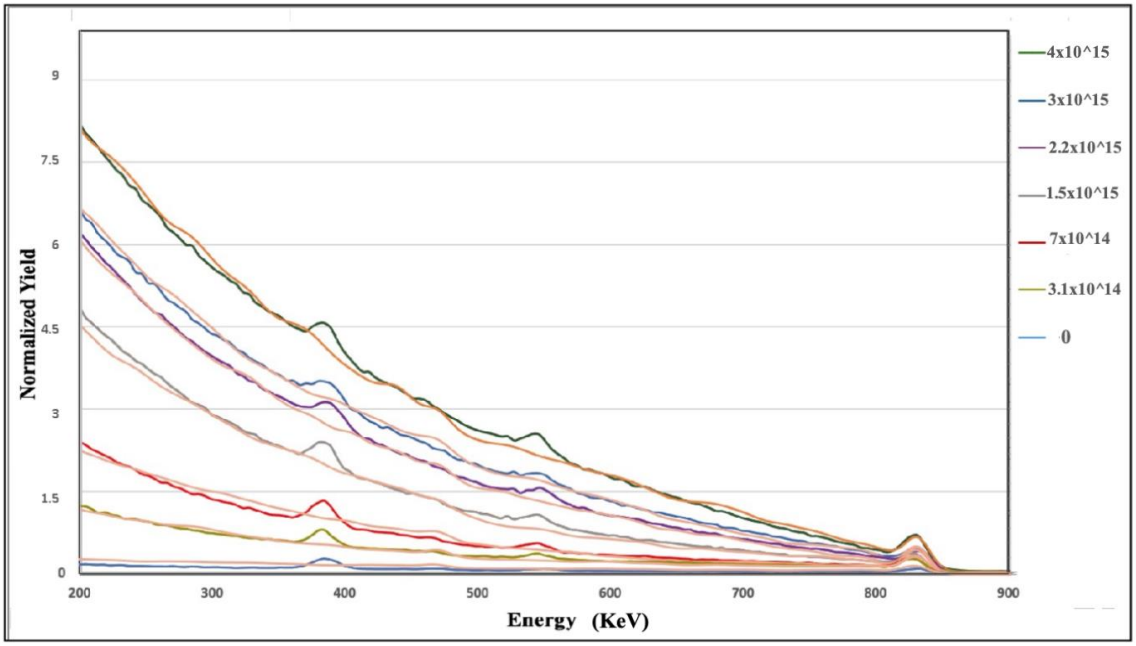


Note: Colored lines show experimental spectra, and orange lines represent the best fit from McChasy simulations.

As shown in Scheme 3.4, ion irradiation causes a peak at an energy of approximately 820 to 853 keV, also known as the "damage peak" This peak results from the direct backscattering of He ions on AlN atoms, which were randomly displaced by implantation with $Au^+$ ions through elastic nuclear interaction.

As shown in Scheme 3.4 the RBS/C yield exhibited a notable acceleration, and a qualitative analysis indicates a probability of amorphization occurring at the higher fluences. This is attributed to the displacement damage cascades resulting from the implantation of heavy ions into the AlN crystals, which can lead to amorphization in certain materials. The evolution of the RBS/C spectra at this stage strongly suggests the potential for amorphization to occur. [58] Based on multiple simulation runs, the McChasy code simulations (as depicted in Figure 3.2) show a strong alignment with the RBS experimental data collected. Notably, the disorder resulting from irradiation on AlN samples is consistent across all fluences.

### 3.3 Extraction of the damage-depth experimental profile of the crystals

Scheme 3.5 (a) illustrates the progression of the damage-depth profile, represented as the percentage of defects, corresponding to varying ion fluence levels as derived from Monte Carlo simulations. As depicted in Scheme 3.5 (a), negligible damage is observable in the pristine AlN crystal, with a discernibly small amount becoming apparent at an ion fluence of $\varphi_1 = (3.1x10^{14}\ cm^{-2})$. However, a consistent augmentation of disorder within the implanted region is evident with escalating ion fluence levels, culminating in the most pronounced shift in damage occurring at a depth of ≈650nm across all AlN crystals, and for ion fluence of $\varphi_3 = (1.5x10^{15}\ cm^{-2})$, a wide shift in damage occurring at a depth of ≈300nm starts to occur.

The progression of damage, as depicted in Scheme 3.5 (a), exhibits an initial rapid increase within the first three AlN crystal samples ($\varphi_1 = (3.1x10^{14}\ cm^{-2})$, $\varphi_2 = (7x10^{14}\ cm^{-2})$, $\varphi_3 = (1.5x10^{15}\ cm^{-2})$, followed by a slower rate of increase in the subsequent three samples compared to the initial ones. Notably, there is a convergence in the damage values between $\varphi_5 = (3x10^{15}\ cm^{-2})$ and $\varphi_6 = (4x10^{15}\ cm^{-2})$, indicating that the sample has nearly reached a state of saturation. Consequently, introducing a new sample with a higher fluence is likely to result in minimal additional damage compared to $\varphi_6 = (4x10^{15}\ cm^{-2})$.

The observed damage is likely to consist of Frenkel pairs, small defect clusters, or possibly amorphous regions formed due to displacement cascades. However, Rutherford backscattering spectroscopy (RBS/C) alone cannot definitively identify these defect types. A more detailed analysis would require varying the probing ion energies to gain deeper insights. Such investigations, however, demand considerable beam time, which exceeds the scope of the current study. The maximum damage kinetics for each fluence was plotted against the percent of damage as shown in Scheme 3.5 (b), (c). In Scheme 3.5 (b) the rapid increase in the damage can be seen clearly at 0.5 µm, in Scheme 3.5 (c) the rapid increase in the damage can be seen until 13 as a percentage of defects at 1µm after that a slower rate of increase can be seen as mentioned before.

**Scheme 3.5**

*Extraction of the damage-depth experimental profile of the crystals*

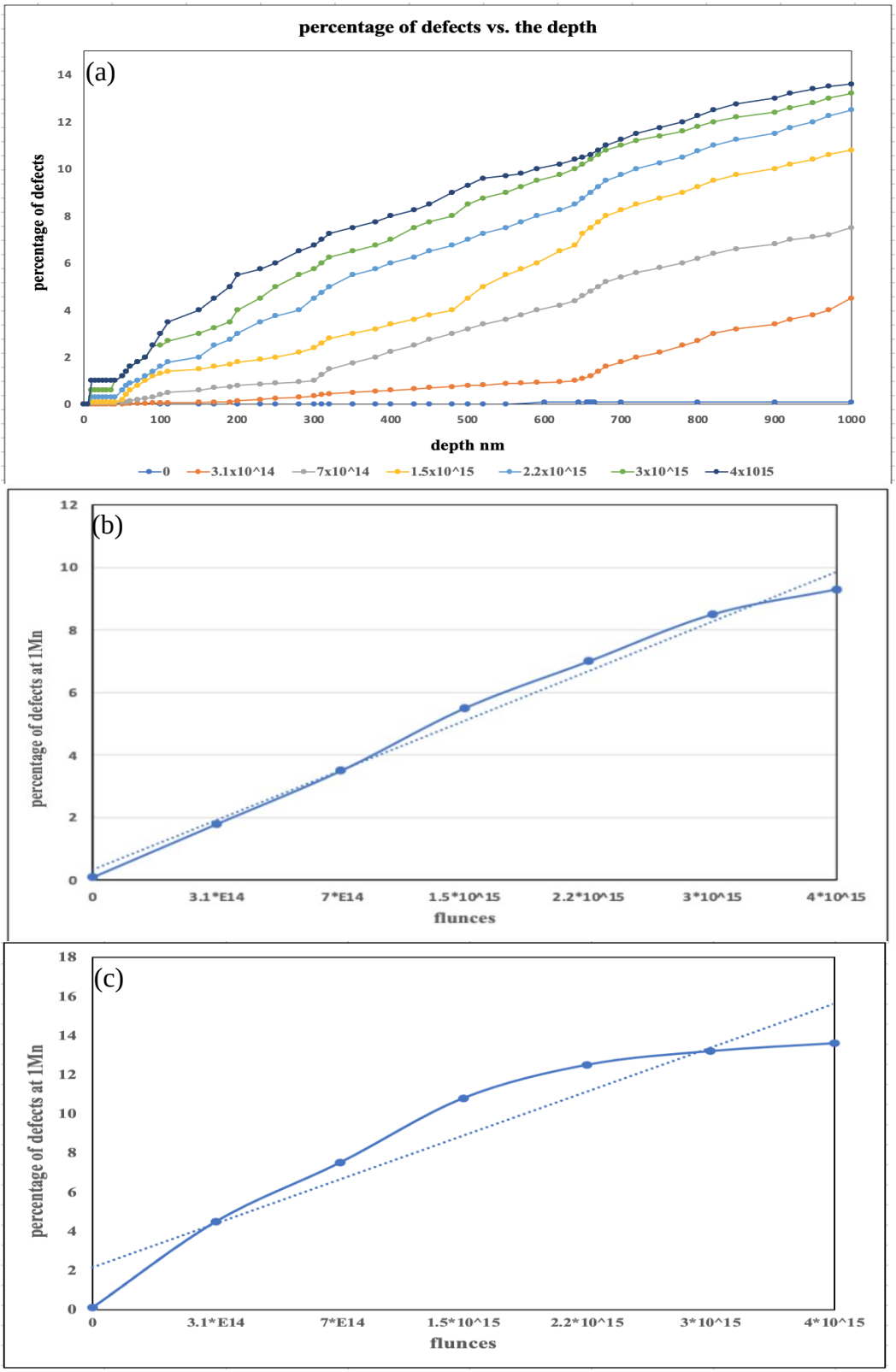


Note: (a) Damage-depth profiles of AlN crystals implanted with 6 MeV Au+ ions at room temperature, with damage levels in % of defects simulated by McChasy for each fluence. (b) Maximum damage kinetic vs. defect percentage at 0.5 µm. (c) Maximum damage kinetic vs. defect percentage at 1 µm.

### 3.4 XRD and TEM results

A cross-sectional TEM study was conducted on an AlN sample implanted at room temperature with 6 MeV Au ions to a fluence of $7.4 \times 10^{14}$ $cm^{-2}$. The results are illustrated in Fig. 3.1.

Images taken in two-beam conditions using g = 0002 are displayed in Fig 3.1(c), The "g" represents a reciprocal lattice vector corresponding to a diffraction spot. The notation "g = 0002" indicates the second-order diffraction condition along the [0002] direction in the crystal, which is crucial for imaging particular crystallographic planes and defect features in the material under investigation. Both the Au concentration profile and the vacancy concentration profile calculated by SRIM are also displayed in Fig 3.1(c). In this figure, a bright field image shows dark dot-like defects from the surface up to a depth of around 1600 nm. A gradient of concentration of defects is observed with a lower concentration close to the surface, and a higher concentration in the rear part of the damaged layer. But the surface layer seems already populated by a rather high defect density, as far as it can be judged.

Contrary to the He and Al implantations, the defect layer appears to be significantly larger compared to the predictions of SRIM, as clearly shown in Fig 3.1. This is probably the result of the inaccuracy of SRIM calculations in the present conditions as it has already been shown that SRIM does not predict accurately for high energy - high mass projectiles on light targets.

Micrographs taken in two beam conditions using g = 1-100 are depicted in Fig 3.1(a) (b). Almost nothing is observed in bright field conditions in Fig 3.1(a). In the weak-beam dark field conditions shown in Fig 3.1 (b), only a faint light contrast seems to be observed in a deep layer, up to 1600 nm in depth, but by looking more closely, defects are already visible in the near-surface region.

**Figure 3.1**

*Cross-sectional TEM micrographs of an AlN layer after 6 MeV Au implantation at RT (7.4x10¹⁴ cm⁻²)*

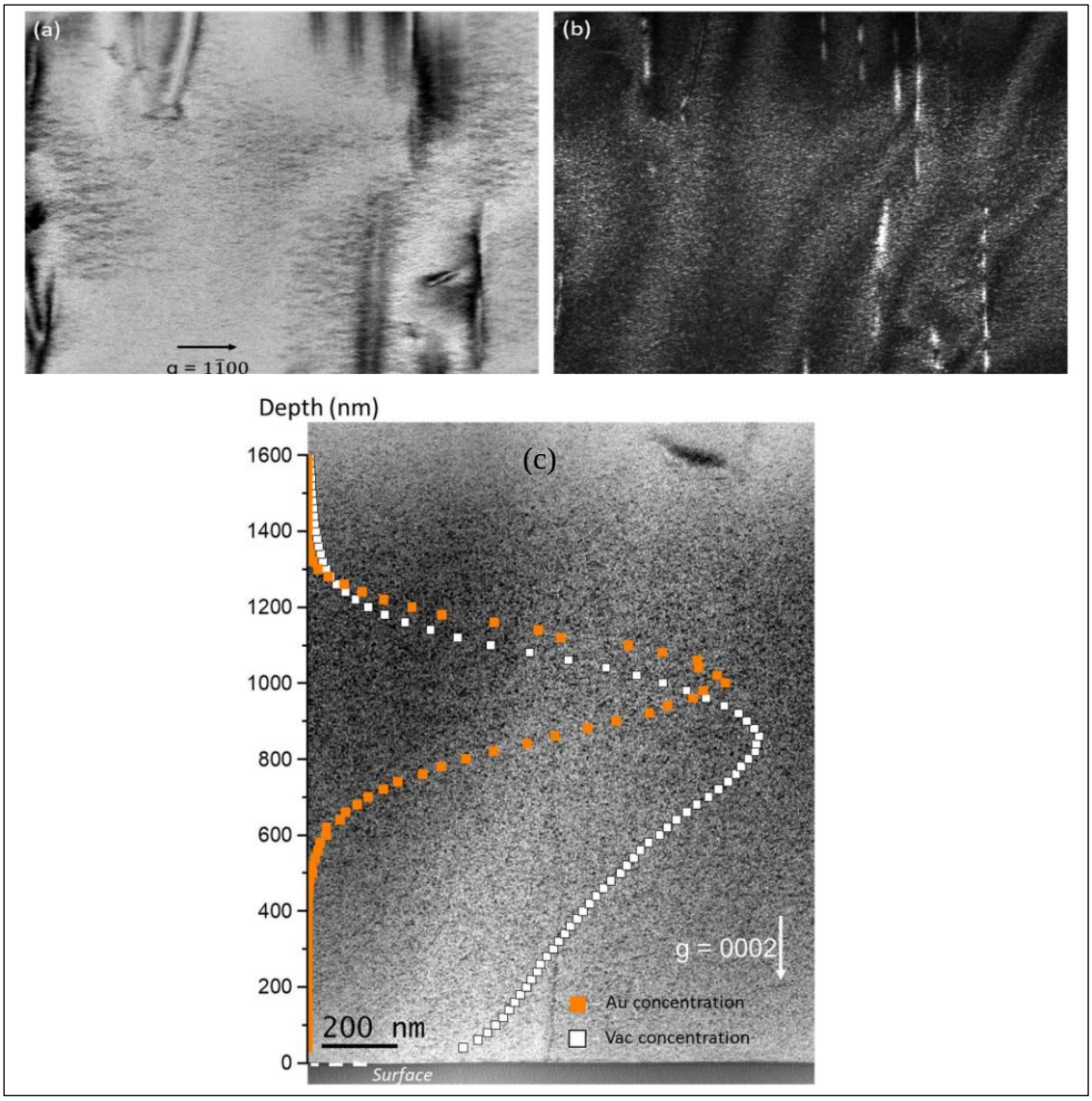


Note: (a) and (b) show bright field and weak beam dark field images (g = 1-100). (c) Bright field TEM image (g = 0002) with SRIM-calculated vacancy and Au ion profiles in white and orange.

XRD curves obtained after Au implantation at room temperature on AlN samples are reported in Fig 3.2. The samples were implanted to fluences ranging from $3x10^{14}$ to $5.4x10^{15}$ $cm^{-2}$. The sample implanted to the highest fluence of $5.4x10^{15}$ $cm^{-2}$ was implanted with a higher flux as compared to the other fluences, a small increase in the temperature could be detected during implantation, which may have induced some relaxation processes in this specimen.

Nevertheless, the strain values obtained for this specimen are in line with the trends observed at lower fluence, and consequently, the results for this specimen are included in the following description. Elastic strains for the near-surface region and at maximum are reported for all fluences in Table 3.3 and plotted as a function of the fluence in Fig 3.2.

**Table 3.3**

*Elastic strains for the near-surface region and at maximum are reported for all fluences*

| Au ion fluence ($cm^{-2}$) | Surface | $\varepsilon_s$ (%) | Max dpa | $\varepsilon_M$ (%) |
|---|---|---|---|---|
| $3 \times 10^{14}$ | 0.20 | 0.55 | 0.5 | 0.5 |
| $7 \times 10^{14}$ | 0.50 | Ø | 1.15 | 1.25 |
| $1.5 \times 10^{15}$ | 1 | 1.25 | 2.45 | 1.80 |
| $2.2 \times 10^{15}$ | 1.5 | 1.40 | 3.55 | 2.00 |
| $3 \times 10^{15}$ | 2 | 1.60 | 4.85 | 2.20 |
| $4 \times 10^{15}$ | 2.65 | $1.75 \pm 0.1$ | 6.45 | 2.45 |
| $5.4 \times 10^{15}$ | 3.60 | $1.65 \pm 0.15$ | 8.70 | 2.45 |

Note: with εN the strain normal to the sample surface, and εM the maximum strain.

As for the Al implantation, the determination of the near-surface strain in the Au-implanted specimens is not always straightforward due to the many various shapes of the near-surface satellite peaks on XRD curves. It could not be determined for the fluence $7x10^{14}$ $cm^{-2}$ and an error bar is given with the near-surface strain values of the samples implanted to $4x10^{15}$ and $5.4x10^{15}$ $cm^{-2}$. This, however, does not prevent the observation of an obvious tendency.

Fig 3.2 and Scheme 3.6 show an increase of the strain values with the fluence in both regions, which is expected considering the increase of the nuclear-deposited energy. Indeed, with increasing fluence, a steady strain increase is observed in both regions before slowing down and reaching saturation. The strain values at saturation are estimated to be close to 1.7% and 2.5% for the near-surface region and the peak damage region, respectively, as shown in Scheme 3.6.

**Figure 3.2**

*X-ray intensity distribution around the (0001) reflection of AlN templates implanted with 6 MeV Au ions at room temperature, with fluences from 3×10¹⁴ to 5.4×10¹⁵ cm⁻²*

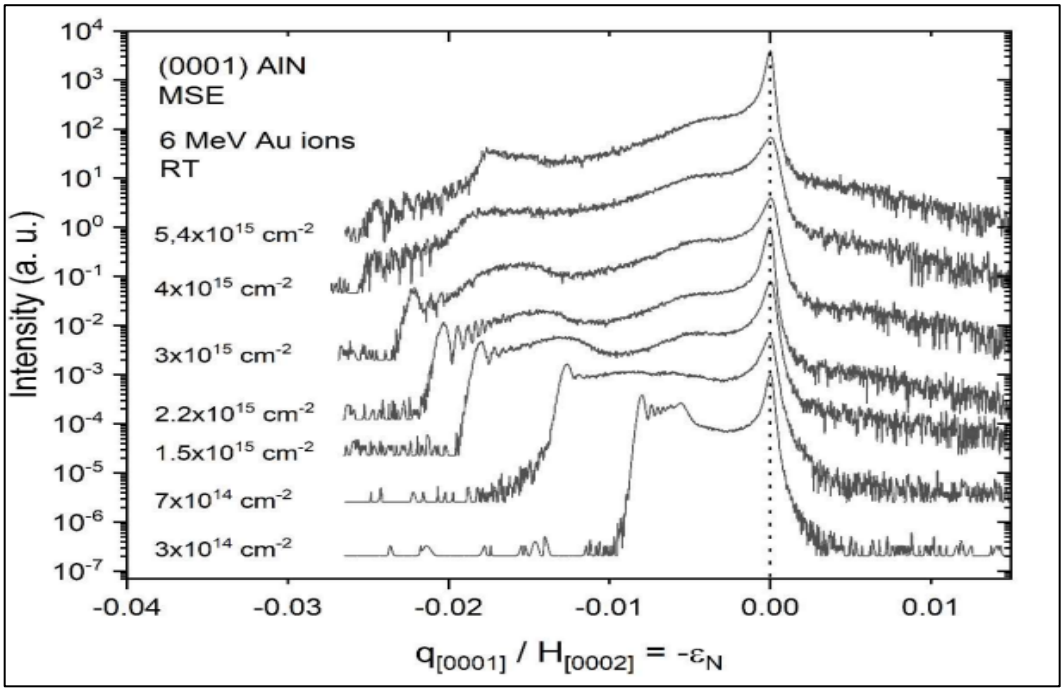


Note: The x-axis shows -εN (strain normal to the surface), and intensity is in arbitrary units.

**Scheme 3.6**

*Elastic strain values were estimated from XRD curves vs. fluence for Au implantation at room temperature in AlN samples, with εS (near-surface) and εM (maximum) reported*

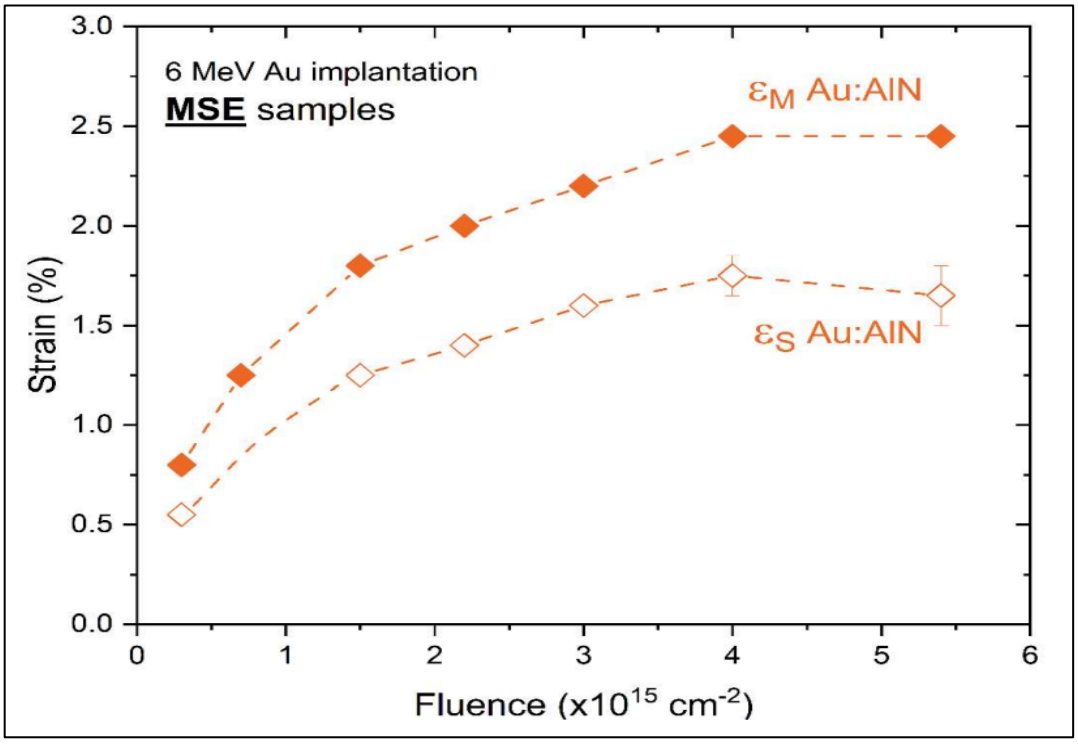

### 3.5 Conclusions

The effect of helium ions on the structure of aluminum nitride (AlN) single crystals was studied in detail using $Au^+$ ions. The crystals were implanted with 6 MeV $Au^+$ ions and analyzed using the Rutherford Backscattering in Channeling (RBS/C) technique. Various ion fluences were used to mimic the damage created by heavy recoil nuclei.

Using 6 MeV $Au^+$ ions at varying fluences, RBS/C analysis revealed a gradual increase in damage, measured as a percentage of defects, reaching a saturation point at approximately 13% at a depth of 1 μm. The convergence of damage values between $\varphi_5 = 3 \times 10^{15}$ cm$^{-2}$ and $\varphi_6 = 4 \times 10^{15}$ cm$^{-2}$ suggests defect saturation, consistent with findings by Wesch and Wendler (2016) on wide-bandgap materials [59]. Depth-dependent damage profiles align with studies like Toulemonde et al. (2012), showing concentrated displacement damage at specific depths caused by heavy ions [60].

Complementary techniques, including TEM and XRD, revealed a gradient in defect concentration, with higher densities near the rear of the damaged layer and significant surface damage. XRD analysis indicated elastic strain saturation at approximately 1.7% near the surface and 2.5% at peak damage regions, highlighting AlN's robust structural behavior. The discrepancy between observed defect sizes and SRIM predictions underscores the limitations of SRIM for high-energy, heavy-ion impacts on light materials.

The hypothesis of defects manifesting as Frenkel pairs, defect clusters, or small amorphous regions aligns with previous studies by Reinhard, Brian (2015) [61]. The observed rapid damage increase at lower fluences, followed by deceleration at higher fluences, mirrors findings by Napolitani, Enrico.(2015) on defect recombination and saturation mechanisms [62]. These results validate the accuracy of Monte Carlo McChasy simulations in predicting damage profiles and emphasize the need for complementary techniques, such as positron annihilation spectroscopy, for detailed defect characterization.

Overall, the findings highlight AlN's resilience to radiation-induced damage, reinforcing its suitability for radiation-intensive applications. This study advances our understanding of structural changes under heavy ion implantation and contributes to the development of

predictive models for radiation damage in materials. Further investigations using varied ion energies and extended methodologies are recommended to refine defect characterization and explore material behavior under extreme conditions.

### 3.6 Future perspectives

1. Conduct implantation experiments at varying temperatures to explore temperature-dependent effects on the material.
2. Evaluate the optical density of vacancies both before and after implantation to understand changes in defect states.
3. Investigate the stability of the crystal post-implantation to assess its structural and functional resilience.

# List of Abbreviations

| Abbreviation | Meaning |
|---|---|
| ITER | International Thermonuclear Experimental Reactor |
| LEDs | light-emitting diodes |
| RBS | Rutherford Backscattering Spectrometry |
| RBS/C | Rutherford Backscattering Spectrometry by Channeling mode |
| IBA | Ion Beam Analysis |
| JANNuS | Joint Accelerators for Nanoscience and Nuclear Simulation |
| XRD | X-ray diffraction |
| TEM | Transmission Electron Microscope |
| VESTA | Visualization of Electron/Nuclear and Structures Analysis |
| SRIM | Stopping and Range of Ions in Matter |
| RUMP | Rutherford Universal Manipulation Program |
| McChasy | Monte Carlo Channeling Simulation code |
| ERDA | elastic recoil detection analysis |
| CHIMèNE | Chemistry, Irradiation, Materials, Modeling, and Electrochemistry for Nuclear Energy |
| dpa | displacements per atom |

# References


1. Holmes-Siedle, A. (2003). *Encyclopedia of Physical Science and Technology: Radiation Effects in Electronic Materials and Devices*. doi:10.1016/B0-12-227410-5/00644-X

2. Schunck, N., & Regnier, D. (2022). Theory of nuclear fission. *Progress in Particle and Nuclear Physics*. doi:10.1016/j.ppnp.2022.103963

3. Lewis, E. E. (2008). *Fundamentals of Nuclear Reactor Physics*. Academic Press.

4. Atzeni, S., & Meyer-ter-Vehn, J. (2004). Nuclear fusion reactions. *The Physics of Inertial Fusion*. Oxford University Press. ISBN 978-0-19-856264-1.

5. ITER. (2024, May 24). Retrieved from https://www.iter.org

6. Mancusi, D., Charity, R., & Cugnon, J. (2010). Unified description of fission in fusion and spallation reactions. *Physical Review C, 82*, 044610. doi:10.1103/physrevc.82.044610

7. World Nuclear Association. (n.d.). Nuclear power in the world today. Retrieved from https://world-nuclear.org/information-library/current-and-future-generation/nuclear-power-in-the-world-today.aspx

8. Matzke, H. J. (1992). Radiation damage in nuclear materials. *Nuclear Instruments and Methods in Physics Research Section B: Beam Interactions with Materials and Atoms, 65*(1–4), 30–39. doi:10.1016/0168-583x(92)95010-o

9. Energy Education. (2022). Alpha decay. Retrieved from https://energyeducation.ca/encyclopedia/Alpha_decay

10. U.S. Nuclear Regulatory Commission. (2024, May 24). Medical uses of nuclear materials. Retrieved from https://www.nrc.gov/materials/medical.html

11. Allen, T., Busby, J., Meyer, M., & Petti, D. (2010). Materials challenges for nuclear systems. *Materials Today, 13*(12), 14–23. doi:10.1016/s1369-7021(10)70220-0

12. Kumar, S., Reshi, B. A., & Varma, R. (2018). Comparison of silicon, germanium, gallium nitride, and diamond for use as a detector material in experimental high-energy physics. *Results in Physics, 9*, S2211379718312658. doi:10.1016/j.rinp.2018.08.045

13. Tekin, H. O., & Kilicoglu, O. (2020). The influence of gallium (Ga) additive on nuclear radiation shielding effectiveness of Pd/Mn binary alloys. *Journal of Alloys and Compounds, 815,* 152484. doi:10.1016/j.jallcom.2019.152484

14. Ionescu, G. C., Nae, I., Ripeanu, R. G., Dinita, A., & Stan, G. (2017). Studies on tribological behavior of aluminum nitride-coated steel. *IOP Conference Series: Materials Science and Engineering, 174*, 012052. doi:10.1088/1757-899X/174/1/012052

15. Wakai, E., Takaya, S., et al. (2021). Irradiation damages of structural materials under different irradiation environments. *Journal of Nuclear Materials, 543*, 152503. doi:10.1016/j.jnucmat.2020.152503

16. Gibbons, J. F. (1972). Ion implantation in semiconductors—Part II: Damage production and annealing. *Proceedings of the IEEE, 60*(9), 1062–1096. doi:10.1109/PROC.1972.8854

17. Meissner, T., & Medjdoub, F. (2024, May 24). Aluminum nitride substrates. Retrieved from http://www.inrel-npower.eu/sites/default/files/T03_Meissner_Medjdoub.pdf

18. Reeve, K. D. (1975). Ceramics as nuclear reactor fuels. *Ceramic International, 1*(2), 59–71. doi:10.1016/0390-5519(75)90008-3

19. Alsaad, A. M., Al-Bataineh, et al. (2020). Measurement and ab initio investigation of structural, electronic, optical, and mechanical properties of sputtered aluminum nitride thin films. *Frontiers in Physics, 8*. doi:10.3389/fphy.2020.00115

20. Xu, Runjie Lily, Muñoz Rojo, et al. (2019). Thermal conductivity of crystalline AlN and the influence of atomic-scale defects. *Journal of Applied Physics, 126*(18), 185105. doi:10.1063/1.5097172

21. Jublot-Leclerc, S., Bouhali, G., Pallier, F., & Declémy, A. (2021). Temperature dependence of elastic strain and damage build-up in He implanted AlN. *Journal of the European Ceramic Society, 41*(1), 259–267. doi:10.1016/j.jeurceramsoc.2020.08.010

22. Hexatech Inc. (2024, May 24). AlN growth process. Retrieved from https://www.hexatechinc.com/aln-growth-process.html

23. Kogut, Iurii, Hartmann, et al. (2019). Electromechanical losses in carbon- and oxygen-containing bulk AlN single crystals. *Solid State Ionics, 343*, 115072. doi:10.1016/j.ssi.2019.115072

24. Krishnan, Kannan M. (2021). Introduction to materials characterization, analysis, and metrology. In *Principles of Materials Characterization and Metrology*. Oxford Academic. doi:10.1093/oso/9780198830252.003.0001

25. Williams, J. S., & Bird, J. R. (1989). 1 - Concepts and principles of ion beam analysis. In *Academic Press*, pp. 3–102.

26. Huddle, James R., Grant, Patrick G., Ludington, Alexander R., & Foster, Robert L. (2007). Ion beam-induced luminescence. *Nuclear Instruments and Methods in Physics Research Section B: Beam Interactions with Materials and Atoms, 261*(1–2), 475–476.

27. Wikipedia. (n.d.). Rutherford backscattering spectrometry. Retrieved from https://en.wikipedia.org/wiki/Rutherford_backscattering_spectrometry

28. Ntemou, E., Kokkoris, M., Lagoyannis, A., Preketes-Sigalas, K., & Tsavalas, P. (2019). Differential elastic scattering cross sections for deuterons on 9Be, at energies and angles suitable for elastic backscattering spectroscopy. *Nuclear Instruments and Methods in Physics Research Section B: Beam Interactions with Materials and Atoms*. doi:10.1016/j.nimb.2019.08.032

29. Salih, M. (2020). Student thesis: bAppP 2020. Retrieved from https://fse.studenttheses.ub.rug.nl/22880/1/bAppP_2020_SalihM.pdf

30. Mayer, M. (2003). Rutherford backscattering spectrometry (RBS). In *Workshop on Nuclear Data for Science and Technology: Materials Analysis*.

31. Mayer, M. (2003). Rutherford backscattering spectrometry (RBS). Retrieved from https://www.nuclear.lu.se/fileadmin/nuclear/Undervisning/TillSubFys/RBS-Mayer_1.pdf

32. Epp, J. (2016). Materials characterization using nondestructive evaluation (NDE) methods: X-ray diffraction (XRD) techniques for materials characterization. doi:10.1016/b978-0-08-100040-3.00004-3

33. Bunaciu, Andrei A., Udriştioiu, Elena Gabriela, & Aboul-Enein, Hassan Y. (2015). X-ray diffraction: Instrumentation and applications. *Critical Reviews in Analytical Chemistry, 45*(4), 289–299. doi:10.1080/10408347.2014.949616

34. Singh, Ashok K. (2016). Experimental methodologies for the characterization of nanoparticles. In *Engineered Nanoparticles*. doi:10.1016/B978-0-12-801406-6.00004-2

35. Jozwik, P., et al. (2020). Advanced Monte Carlo simulations for ion-channeling studies of complex defects in crystals. In *Theory and Simulation in Physics for Materials Applications: Cutting-Edge Techniques in Theoretical and Computational Materials Science, 296*, 133.

36. Wilson, A. J. C. (1984). Symposium on crystallographic statistics. *International Union of Crystallography International Congress* (13th: Hamburg, Germany).

37. JP-Minerals. (2024, May 24). VESTA: Visualization for Electronic and Structural Analysis. Retrieved from https://jp-minerals.org/vesta/en/

38. Bernas, H., Chaumont, J., Cottereau, E., Moroy, G., Clerc, C., Kaïtasov, O., Ledu, D., & Salomé, M. (1992). Progress report on ARAMIS, the 2 MV tandem at Orsay. *Nuclear Instruments and Methods in Physics Research Section B, 62*, 416–420. doi

39. Chaumont, J., Lalu, F., Salomé, M., Lamoise, A.-M., & Bernas, H. (1981). A medium energy facility for variable temperature implantation and analysis. *Nuclear Instruments and Methods, 189*, 193–198. doi

40. Ion Beam Centers. (2024, May 24). Ion beam software resources. Retrieved from https://www.ionbeamcenters.eu/resources/ion-beam-software/

41. Turcaud, J. A., Schuur, J., & Pong, R. (2022). Ion implantation simulation and optimization in semiconductor compounds. *CS MANTECH Conference*.

42. Robinson, M., & Torrens, I. (1974). Computer simulation of atomic-displacement cascades in solids in the binary-collision approximation.

43. Ziegler, J. F., Ziegler, M. D., & Biersack, J. P. (2010). SRIM – The stopping and range of ions in matter. *Nuclear Instruments and Methods in Physics Research Section B: Beam Interactions with Materials and Atoms, 268*(11–12), 1818–1823. Retrieved from http://www.srim.org (Accessed: May 24, 2024).

44. Mamalakis, E. (2019). Data analysis of RBS spectra using differential evolution.

45. International Centre for Theoretical Physics. (2019). Data analysis of RBS spectra using differential evolution. Retrieved from https://indico.ictp.it/event/a08139/session/4/contribution/3/material/0/1.pdf.

46. Moretto, P., & Razafindrabe, L. (1995). Simulation of RBS spectra for quantitative mapping of inhomogeneous biological tissue. *Nuclear Instruments and Methods in Physics Research Section B: Beam Interactions with Materials and Atoms, 95*(4), 557–562. doi:10.1016/0168-583x(95)00444-0

47. Jóźwik, P., et al. (2013). Analysis of crystal lattice deformation by ion channeling. *Acta Physica Polonica A, 123*(5), 828–830.

48. Nowicki, L., Jagielski, J., Mieszczyński, C., Skrobas, K., Jóźwik, P., & Dorosh, O. (2021). McChasy2: New Monte Carlo RBS/C simulation code designed for large crystalline structures. *Nuclear Instruments and Methods in Physics Research Section B: Beam Interactions with Materials and Atoms*. doi:10.1016/j.nimb.2021.04.004

49. Jóźwik, P., Nowicki, L., Ratajczak, R., Stonert, A., Mieszczyński, C., Turos, A., Morawiec, K., Lorenz, K., & Alves, E. (2019). Monte Carlo simulations of ion channeling in crystals containing dislocations and randomly displaced atoms. *Journal of Applied Physics, 126*(19), 195107. doi:10.1063/1.5111619

50. Mosaic IJCLab. (2024, May 24). Resources on material characterization. Retrieved from https://mosaic.ijclab.in2p3.fr.

51. MTI Corporation. (2024, May 24). Aluminum nitride substrates. Retrieved from https://www.mtixtl.com/aluminumnitridesubstratesaln.aspx.

52. Schroder, D. K. (2006). *Semiconductor Material and Device Characterization.* Wiley.

53. Ishikawa, K., et al. (2000). Defect formation in AlN single crystals by ion implantation. *Nuclear Instruments and Methods in Physics Research Section B: Beam Interactions with Materials and Atoms, 166–167,* 557–562.

54. Chu, W. K., Mayer, J. W., & Nicolet, M. A. (1978). *Backscattering Spectrometry.* Academic Press.

55. Nord, J., et al. (2001). Amorphization mechanisms of crystalline materials under ion irradiation. *Journal of Applied Physics, 89*(5), 3128–3135.

56. Wesch, W., & Wendler, E. (Eds.). (2016). *Ion Beam Modification of Solids.* Springer Series in Surface Sciences. doi:10.1007/978-3-319-33561-2

57. Khalfaoui, N., Stoquert, J. P., Haas, F., Traumann, C., Meftah, A., & Toulemonde, M. (2012). Damage creation threshold of $Al_2O_3$ under swift heavy ion irradiation. *Nuclear Instruments and Methods in Physics Research Section B, 286*, –. doi:10.1016/j.nimb.2011.11.047

58. Reinhard, B., Tittmann, B. R., & Suprock, A. (2015). Nuclear radiation tolerance of single-crystal aluminum nitride ultrasonic transducer. *Physics Procedia, 70*, 609–613. doi:10.1016/j.phpro.2015.08.036

59. Napolitani, E. (2015). Ion implantation defects and shallow junctions in Si and Ge. In *Defects in Semiconductors (Semiconductors and Semimetals, Volume 91)* (pp. 93–122). doi:10.1016/bs.semsem.2015.01.00

جامعة النجاح الوطنية
كلية الدراسات العليا

# وصف الضرر في بلورات نيتريد الألومنيوم المفردة بواسطة (RBS-C)، تقنية تحليل شعاع أيون

إعداد
سراب عواد حسين

إشراف
أ. د. إسماعيل وراد
د. أحمد بصلات

قدمت هذه الرسالة استكمالا لمتطلبات الحصول على درجة الماجستير في الكيمياء، من كلية الدراسات العليا، في جامعة النجاح الوطنية، نابلس – فلسطين.

2024

# وصف الضرر في بلورات نيتريد الألومنيوم المفردة بواسطة (RBS-C)، تقنية تحليل شعاع أيون

**إعداد**

**سراب عواد حسين**

**إشراف**

**أ. د. إسماعيل وراد**

**د. أحمد بصلات**

## الملخص

تلعب المواد العازلة والبصرية مثل نيتريد الألومنيوم (AlN) دوراً حاسماً في مفاعلات الاندماج المستقبلية، وخاصة في الأنظمة التشخيصية. يتم النظر في استخدام AlN كطلاء عازل في بعض تصميمات المفاعلات نظراً لمقاومته العالية للتآكل الكيميائي وأيضاً لامتلاكه موصلية حرارية عالية تصل إلى 321 واط/متر.ك. فهم آليات تدهور AlN تحت تأثير الزرع والإشعاع يعتبر ذا أهمية قصوى.

هذه الدراسة حققت في تأثير أيونات الهيليوم على بنية بلورات نيتريد الألومنيوم (AlN) الأحادية باستخدام أيونات $Au^+$ بقدرة 6 ميغا إلكترون فولت. تم زرع البلورات بأيونات $Au^+$ وتحليلها باستخدام تقنية التشتت العكسي لرذرفورد في التوجيه القنوي (RBS/C) عبر عدة كثافات أيونية لمحاكاة الضرر الناتج عن النوى الثقيلة المرتدة. أظهرت النتائج زيادة تدريجية في الضرر، مُقاساً كنسبة مئوية للعيوب، مع زيادة كثافة الأيونات، ووصولها إلى حد التشبع عند عمق حوالي 1.3 ميكرومتر. أكدت محاكاة مونت كارلو McChasy دقة بيانات RBS/C التجريبية، مما يدل على توافق ممتاز.

أظهرت ملاحظات المجهر الإلكتروني النافذ (TEM) لعينات AlN المزروعة مسبقاً بأيونات $Au^+$ بقدرة 6 ميغا إلكترون فولت في درجة حرارة الغرفة وجود تدرج في تركيز العيوب، مع كثافات أعلى في الجزء الخلفي من الطبقة المتضررة وكثافة عيوب عالية بشكل ملحوظ عند السطح. أشارت التباينات بين أحجام العيوب المرصودة وتوقعات SRIM إلى محدودية SRIM في حالة القذائف ذات الطاقة العالية والكتلة

العالية على الأهداف الخفيفة. قدم تحليل حيود الأشـــعة الســـينية (XRD) رؤى حول قيم الإجهاد المتأثرة بكثافة وجرعة الزرع.

على الرغم من الزيادة الطفيفة في درجة الحرارة في العينة ذات الكثافة الأعلى، بقيت قيم الإجهاد ثابتة مع الكثافات المنخفضة، مما يشير إلى سلوك قوي. زادت الإجهادات المرنة مع كثافة الزرع، ووصلت إلى حد التشبع عند حوالي 1.7% و2.5% لمناطق الضرر السطحي والقمي، على التوالي. تم ملاحظة تحديات في تحديد الإجهاد السطحي بسبب أشكال منحنيات XRD المعقدة، ولكن لوحظ اتجاه عام.

تقدم هذه الدراسة رؤى قيمة حول التغيرات الهيكلية التي يسببها الهيليوم في بلورات AlN، مما يعزز فهمنا لاستجابات المواد للإشعاع ويساعد في تطوير نماذج تنبؤية للضرر الناجم عن الإشعاع في المواد.

**الكلمات المفتاحية:** بلورات نيتريد الألومنيوم؛ زرع الأيونات؛ مطيافية التشتت العكسي لرذرفورد في التوجيه القنوي (RBS/C)؛ شفرة محاكاة مونت كارلو McChasy؛ العيوب؛ الإجهاد؛ أيونات $He^+$؛ أيونات $Au^+$